

Research papers

Autoregressive model-based parameter correlation for state of charge and state of health of lithium-ion batteries using built-in piezoelectric transducer induced ultrasonic waves



Shabbir Ahmed ^{a,b} *, Saman Farhangdoust ^{a,c} , Fu-Kuo Chang ^a

^a Structures and Composites Laboratory (SACL), Department of Aeronautics and Astronautics, Stanford University, Stanford, CA, USA

^b Department of Mechanical Engineering, South Dakota State University, Brookings, SD, USA

^c Aerospace Engineering Department, Embry-Riddle Aeronautical University, Daytona Beach, FL, USA

ARTICLE INFO

Keywords:
Guided waves
Autoregressive model
Modal analysis
State of charge
State of health
Lithium-ion battery

ABSTRACT

It is crucial to accurately monitor the performance, health, and lifespan of lithium-ion batteries to ensure reliable, efficient, and on-demand delivery of stored electrical energy for hybrid and electric vehicle technologies. This paper presents a method to monitor the state of charge (SoC) and state of health (SoH) of lithium-ion batteries by utilizing ultrasonic guided wave propagation signals. The lithium-ion battery is modeled as a time-varying single-degree-of-freedom vibrating system and the time-varying nature of the system is captured by successive utilization of the time-invariant autoregressive models. The proposed technique focuses on extracting the time-dependent natural frequencies and damping ratios of the lithium-ion batteries from the ultrasonic guided wave signals through the use of autoregressive model-based modal analysis techniques. The extracted natural frequencies and damping ratios are then correlated with the battery SoC and SoH to assess the battery conditions accurately. Lengthwise signals exhibit a decreasing trend in natural frequencies as the SoC increases, whereas, the thickness direction signals show the opposite trend, frequencies increase with rising SoC. This method elucidates the potential of ultrasonic guided wave-based real-time monitoring of battery SoC and SoH in its life cycle.

1. Introduction

Lithium-ion batteries have been widely adopted as a viable source of portable energy storage devices with ubiquitous applications in consumer electronics and electric vehicles such as electric cars, buses, drones, and aircraft [1]. Desirable properties such as high energy density, high energy-to-weight ratio, better operating voltage range, low self-discharge characteristics, and cost-effectiveness have made lithium-ion batteries one of the most favorable candidates for electric vehicles, which require reliable and steady battery performance throughout their service life [2]. As a result, to ensure the safe operation of the battery pack and optimal usage of individual batteries in electric vehicles, a battery management system (BMS) is incorporated that maintains and predicts the status of the battery such as the state of charge (SoC) and state of health (SoH) [3,4]. Additionally, the prediction of remaining useful life and cell balancing for proper operation of the battery pack may also be considered as the task of the battery management system [5–7].

An accurate estimation of the SoC of the battery during operation has been a challenging task as it requires the measurement

of Lithium concentrations in the electrodes [8, Chapter 6] [9–12]. The open circuit voltage (OCV) of the battery may be taken as an indirect measure of the SoC, which tacitly assumes that the cell is in an equilibrium state. However, during battery operation, cells are far from the equilibrium state [13,14]. With coulomb counting, the state of charge can be inferred, however, it requires initial SoC and an accurate current sensor [15,16]. By accurately estimating the Lithium concentrations within the battery, it is possible to have an accurate estimation of the state of charge [17,18]. Experimental determination of the Lithium concentrations during operation is a challenging task. As a result, electrochemical modeling for state estimation is getting attention, which can provide the estimation of Lithium concentrations in the electrodes [19,20]. The drawback of electrochemical modeling is that it requires the solution of a set of partial differential equations which may be computationally expensive and may not be suitable for real-time implementations. To circumvent this problem, model order reduction techniques or surrogate modeling approaches might be sought, which may lessen the computational burden to some extent, with the cost of sacrificing accuracy [21].

* Corresponding author.

E-mail address: shabbir.ahmed@sdstate.edu (S. Ahmed).

Prediction of state of health (SoH) is even more challenging as it entails very slow degradation of the battery [6,22]. SoH is related to the capacity fade of the battery [23]. Capacity fade occurs due to the unwanted side reactions during the charge and discharge process, and some of the lithium ions get trapped into the products of these side reactions [24]. In order to achieve accurate SoH estimation, both model-based techniques and data-driven methods have been proposed. The electrochemical models [25] and equivalent circuit models with their variants [26,27] are two widely used approaches for SoH estimation. By combining these two approaches with the classical state estimation techniques such as Kalman filter, particle filter etc. [28,29], significant improvements have been achieved. In order to estimate the SoH from the voltage and current data, recently, incremental capacity estimation [30], neural network or machine learning-based approaches have been investigated, such as methods based on gated recurrent unit (GRU) [31], long short term memory (LSTM) [32] etc. By combining convolutional neural network (CNN) and LSTM, CNN-Bi-LSTM model was proposed that can achieve accurate SoH estimation under temperature variation [33]. The proposed CNN-Multi-gate Mixture of GRU (CMMOG) model can perform multiple SoH estimation simultaneously [34]. However, these methods are based on voltage and current information and do not take into account the degree of mechanical degradation of the anode and cathode materials.

Under a controlled laboratory environment, a variety of in-situ techniques (X-ray diffraction, X-ray computed tomography, neutron imaging, electrochemical impedance spectroscopy etc.) are available to probe the internal structure and physical evolution of the battery such as the formation of the solid electrolyte interface layer, growth of dendrites, wetting of the electrodes etc [35–38]. However, these techniques may not be suitable for electric vehicle applications as well as for in-service monitoring of the battery. In these respects, an ultrasonic measurement-based battery monitoring approach may provide accurate information on the SoC and SoH of the battery [39–45]. Although an extensive literature exists for the state of charge and state of health estimation of lithium-ion batteries, the present study only focuses on the ultrasonic-based methods. Ultrasonic waves propagating in an elastic medium are strongly affected by the elastic modulus and density of the propagating medium [46–48]. These waves are dispersive in nature, that is, their frequency content change with time [49–51]. Depending on the geometry of the propagating medium and the nature of the excitation used, these waves can propagate in different modes [52]. A number of studies have utilized the time of flight shift of the acoustic wave (stress wave) to determine the state of charge [39]. The time of flight is inversely proportional to the wave speed [53]. It was found that during the charging process, the wave speed monotonically increases with increasing SoC due to the effective increase in the stiffness-to-density ratio of the electrode laminate [54]. In addition to using the time of flight as one of the features, the signal amplitude was also correlated with the state of charge [55,56].

Recently, vibration tests on the battery have been performed to extract the frequency response function of the battery system and to correlate the natural frequency and damping ratio obtained from the frequency response function with the state of charge and state of health of the battery [57–59]. Additionally, the frequency response function can also be used to investigate the cell-to-cell manufacturing variability and stored energy variations [57]. However, for vibration tests, achieving repeatability during reassembling is a challenging task as it is not always possible to position the actuator and the impedance head exactly at the same location. Achieving the correlation with the frequency response function and the state of charge at higher resolutions such as at 1% SoC, 2% SoC, 3% SoC (rather than 1% SoC, 25%SoC, 75% SoC), etc. would require many separate vibration tests to be performed, and the differences between the closely spaced SoC's may not be evident. In this study, improvements have been achieved to remedy these shortcomings by performing modal analysis on the ultrasonic guided wave signals. Additionally, for developing robust algorithms for

efficient monitoring and real-time estimation of SoC and SoH, the use of raw time domain signals may have several limitations such as: (i) the time domain stress wave signal usually contains several peaks. There is no rigorous guideline on which peak should be chosen. The choice of a specific peak may show different amplitude trends and may invoke different interpretations. (ii) The time domain stress wave signal is only amenable to the interpretation of wave propagation phenomenon. It disregards the vibration aspect which may provide additional information for developing robust battery monitoring techniques. The present paper addresses these problems by utilizing techniques from system identification and modal analysis. The complete and raw time domain signal can be compressed into a single value of natural frequency or damping ratio, which has physics-based interpretation. The approach is also amenable to the interpretation of the vibration aspect.

2. Problem statement

No attempt has been made so far to model the dynamics of the time domain ultrasonic guided wave signals from a system's perspective in the context of the lithium-ion batteries and to correlate the extracted dynamic parameters with the state of charge (SoC) and state of health (SoH) of the lithium-ion batteries. This study shows how stress wave signals can be used to estimate the time-varying system parameters (damping ratio and natural frequency) using autoregressive (AR) model-based modal analysis techniques. Finally, it is shown how the system parameters evolve with the change in the SoC and SoH of the battery.

3. Method of approach

3.1. ARX model-based modal analysis

A general n th degree of freedom vibrating structure can be modeled by an ensemble of masses, springs and dampers as below:

$$\mathbf{M}_{[n \times n]} \ddot{\mathbf{q}}(t)_{[n \times 1]} + \mathbf{C}_{[n \times n]} \dot{\mathbf{q}}(t)_{[n \times 1]} + \mathbf{K}_{[n \times n]} \mathbf{q}(t)_{[n \times 1]} = \mathbf{u}(t)_{[n \times 1]} \quad (1)$$

where $\mathbf{q}(t)$ and $\mathbf{u}(t)$ is the generalized displacement and excitation, respectively with dimension $[n \times 1]$. \mathbf{M} , \mathbf{C} , and \mathbf{K} are mass, damping and stiffness matrices respectively with dimension $[n \times n]$. This type of modeling is referred to as the first principle modeling or the models obtained from the laws of physics. For a single degree of freedom vibrating system, $n = 1$, and Eq. (1) can be represented as follows:

$$m \cdot \ddot{q}(t) + c \cdot \dot{q}(t) + k \cdot q(t) = u(t) \quad (2)$$

where, m, c, k represent mass, damping, and stiffness of the single degree of freedom system. Eq. (2) can be modified to write in the following way:

$$\ddot{q}(t) + 2 \cdot \zeta \cdot \omega_n \cdot \dot{q}(t) + \omega_n^2 \cdot q(t) = (u(t)/k) \cdot \omega_n^2 \quad (3)$$

where ζ and ω_n are termed as the damping ratio and natural frequency, respectively, of the single degree of freedom vibrating system. Additionally,

$$\zeta = \frac{c}{c_{crit}}; \quad \omega_n = \sqrt{\frac{k}{m}}; \quad c_{crit} = 2\omega_n m = 2\sqrt{km} \quad (4)$$

where, c_{crit} is the critical damping ratio. The two system parameters, namely: the damping ratio ζ and natural frequency ω_n are unknown constants.

Eq. (1), on the other hand, the same n th degree of freedom vibrating structure can also be modeled by the following autoregressive (AR) with exogenous excitation (X) (ARX) model of order $na = 2n$:

$$y[t] + \sum_{i=1}^{2n} a_i \cdot y[t-i] = \sum_{i=0}^{2n} b_i \cdot x[t-i] + e[t] \quad e[t] \sim \text{iid } \mathcal{N}(0, \sigma_e^2) \quad (5)$$

with t designating its discrete time, $y[t]$ the response signal obtained from the vibrating structure, $x[t]$ the excitation signal, $e[t]$ an (unobservable) uncorrelated (white) innovations sequence with zero mean

and variance σ^2 that generates $y[t]$. a_i and b_i are the model's AR and X parameters which have to be estimated from the available data. $\mathcal{N}(\cdot, \cdot)$ stands for normal distribution with the indicated mean and variance. *iid* stands for independently and identically distributed.

Using the backshift operator $B(B^i \cdot y[t] \triangleq y[t-i])$, the ARX representation of Eq. (5) may be compactly re-written as:

$$\begin{aligned} y[t] + \sum_{i=1}^{2n} a_i \cdot B^i \cdot y[t] &= \sum_{i=0}^{2n} b_i \cdot B^i \cdot x[t] + e[t] \\ \Leftrightarrow A[B] \cdot y[t] &= B[B] \cdot x[t] + e[t], \quad e[t] \sim \text{iid } \mathcal{N}(0, \sigma_e^2) \end{aligned} \quad (6)$$

with

$$A[B] = 1 + \sum_{i=1}^{2n} a_i \cdot B^i \quad B[B] = \sum_{i=0}^{2n} b_i \cdot B^i \quad (7)$$

The transfer function $G(B)$ of the ARX model can be cast as:

$$G(B) = \frac{\sum_{i=0}^{2n} b_i \cdot B^i}{1 + \sum_{i=1}^{2n} a_i \cdot B^i} = \frac{\sum_{i=0}^{2n} b_i \cdot B^i}{\prod_{i=1}^{2n} (1 - \lambda_i \cdot B^i)} \quad (8)$$

$$G(B) = e^{-j\omega T_s} = \frac{\sum_{i=0}^{2n} b_i \cdot e^{-j\omega T_s i}}{\prod_{i=1}^{2n} (1 - \lambda_i \cdot e^{-j\omega T_s i})} \quad (9)$$

where λ_i are the roots of the denominator polynomial and are referred to as the poles of the linear time-invariant (LTI) system. In the absence of an excitation signal, an autoregressive (AR) model can be used and has the following form:

$$y[t] + \sum_{i=1}^{2n} a_i \cdot y[t-i] = e[t] \quad e[t] \sim \text{iid } \mathcal{N}(0, \sigma_e^2) \quad (10)$$

The corresponding transfer function G is as follows:

$$G(B) = e^{-j\omega T_s} = \frac{1}{\prod_{i=1}^{2n} (1 - \lambda_i \cdot e^{-j\omega T_s i})} \quad (11)$$

These roots are related to the natural frequencies and damping ratios of the vibrating structure by the following equations (for discrete-time systems):

$$\omega_{ni} = \frac{|\ln \lambda_i|}{T_s} \quad \zeta_i = -\cos(\angle(\ln \lambda_i)) \quad (12)$$

By using Eq. (12), the natural frequency and damping ratio of Eq. (4) can be estimated from available response ultrasonic wave signals.

3.2. Model parameter estimation

The ARX model of Eq. (5) can be parameterized in terms of the parameter vector $\bar{\theta} = [a_1 \dots a_{na} : b_0, b_1 \dots b_{nb} : \sigma_e^2]^T$ to be estimated from the measured signals, and may be written in linear regression form as:

$$y[t] = \phi^T[t] \cdot \theta + e[t] \quad (13)$$

with

$$\phi[t] = [-y[t-1] \ -y[t-2] \ \dots \ -y[t-na] : x[t] \ x[t-1] \ \dots \ x[t-nb]]^T \quad (14)$$

$$\theta = [a_1 \ \dots \ a_{na} : b_0 \ \dots \ b_{nb}]^T_{[(na+nb+1) \times 1]} \quad (15)$$

and T designating transposition. Then, following substitution of the data for $t = 1, 2, \dots, N$, the following expression is obtained:

$$y = \phi \cdot \theta + e \quad (16)$$

where

$$y := \begin{bmatrix} y[1] \\ \vdots \\ y[N] \end{bmatrix} \quad \phi := \begin{bmatrix} \phi[1] \\ \vdots \\ \phi[N] \end{bmatrix} \quad e := \begin{bmatrix} e[1] \\ \vdots \\ e[N] \end{bmatrix}. \quad (17)$$

Using the above linear regression framework, the estimation of the parameter vector θ is based on the minimization of the weighted least squares (WLS) criterion (a more appropriate criterion compared to

ordinary least squares in view of the Gauss–Markov theorem):

$$J^{WLS} = \frac{1}{N} \sum_{t=1}^N e^T[t] \Gamma_{e[t]}^{-1} e[t] = \frac{1}{N} e^T \Gamma_e^{-1} e \quad (18)$$

which leads to the weighted least squares (WLS) estimator:

$$\hat{\theta}^{WLS} = [\phi^T \Gamma_e^{-1} \phi]^{-1} [\phi^T \Gamma_e^{-1} y]. \quad (19)$$

In these expressions, $\Gamma_e = E\{ee^T\}$ is the residual covariance matrix, which is practically unavailable. Nevertheless, it may be consistently estimated by applying ordinary least squares in the first step. Once the $\hat{\theta}^{WLS}$ has been obtained, the final residual and residual variance can be obtained by:

$$e[t] = y[t] - \phi^T[t] \cdot \hat{\theta}^{WLS} \quad \text{and} \quad \hat{\sigma}_e^2(\hat{\theta}^{WLS}) = \frac{1}{N} \sum_{t=1}^N e^2[t, \hat{\theta}^{WLS}]. \quad (20)$$

The estimator $\hat{\theta}^{WLS}$ may, under mild conditions be shown to be asymptotically Gaussian distributed with mean coinciding with the true parameter vector θ^0 and covariance matrix P_θ :

$$\sqrt{N}(\hat{\theta}_N - \theta^0) \sim \mathcal{N}(\theta, P_\theta) \quad \text{as } N \rightarrow \infty. \quad (21)$$

The overall system identification approach for modal parameter estimation is presented in a compact way in Fig. 1. Akaike information criterion (AIC), Bayesian information criterion (BIC) or the residual sum of squares over the signal sum of squares (RSS/SSS) criterion can be used for model structure selection. For details see Ref. [60].

4. Experimental setup and data collection

In order to correlate the battery's state of charge and state of health with the modal parameters (natural frequency and damping ratio) extracted from the stress wave signals, two types of tests, namely: the electrochemical and ultrasonic wave propagation (stress wave propagation) tests were performed simultaneously as shown in Fig. 2. Tests were conducted on $129 \times 43 \times 5$ mm Lithium-ion pouch cell batteries having a capacity of 3.65 Ah (Model: PL-5545136, AA Portable Power Corp.). The batteries have graphite anode and nickel-manganese-cobalt oxide cathode (NMC chemistry). The nominal voltage of the battery is 3.7 V. The charge and discharge cut-off voltage of the battery are 4.2 V and 3.0 V, respectively. The standard discharge current of the battery is 0.2C with a maximum discharge current of 2C. Electrochemical cycling test was performed using a Neware Battery Test System. The charge–discharge steps were as follows: 1. constant current charging, 2. constant voltage charging, 3. rest, 4. constant current discharge. Four different C-rates were used, namely: C/2, C/3, C/8, and C/10 to study the charging and discharging rate sensitivity on the ultrasonic wave propagation signals. When the battery was undergoing electrochemical cycling, ultrasonic signals were collected every 2-min intervals during the entire time of charging and discharging phase. Four piezoelectric disk transducers (PZT-5A, Acellent Technologies) were permanently installed on the battery. The piezo-transducers had a diameter of 6.35 mm and a thickness of 0.254 mm. Two transducers were mounted on the top and the other two were mounted on the bottom surface of the battery. Hysol Epoxy adhesive was used for mounting the PZT transducers on the battery. After installation, the epoxy was cured for 24 h at the ambient temperature. The layout of the sensors and the battery dimensions are provided in Fig. 3. Ultrasonic signals were collected from three different paths, namely: path 2-1, path 2-3, and path 4-1. Path 2-1 indicates that sensor 2 is the actuator and sensor 1 is the receiver. In path 2-1, ultrasonic waves travel in the longitudinal or length direction of the battery, while in path 2-3 or in path 4-1, waves travel in the thickness direction of the battery.

A 5-peak tone burst hamming windowed signal was used as the excitation signal in the PZT actuator. The center frequency used was from 150 kHz to 700 kHz, with an increment of 25 kHz up to 300 kHz, and a 50 kHz increment after that. Thus, a total of 16 different center

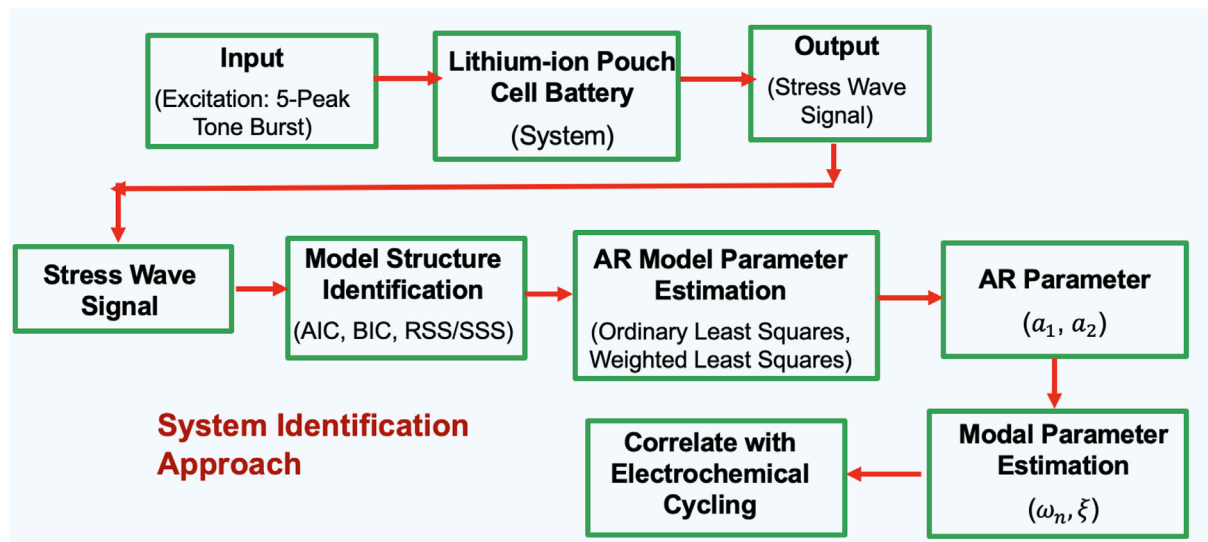


Fig. 1. Flow-chart for modal parameter identification technique from the stress wave propagation signals using an autoregressive model: an output-only system identification approach was adopted.

frequencies were used for exciting the PZT transducers. Scan Sentry data acquisition system manufactured by Acellent Technologies Inc., Sunnyvale, CA was used for the data collection. A sampling frequency of 12 MHz was used during the data collection. Each ultrasonic signal collected had 2000 data points which resulted in 120 μ s long signals. However, after 100 μ s the wave signals are almost dissipated and do not contain any dynamics. As a result, this part of the signal was discarded in the analysis.

5. Autoregressive modeling of Li-ion battery

In this study, the Lithium-ion battery was considered as a single-degree-of-freedom spring mass damper vibrating system at any specific time instant. In fact, the system is a time-varying one, where the damping ratio ζ and natural frequency ω_n are functions of time. However, this time-varying system can be approximated as being multiple time-invariant systems frozen at a sequence of time instants. In this study, the dynamics of Lithium-ion battery at a specific time instant is modeled by Eq. (3), where the system parameter ζ and ω_n are two unknown quantities and need to be estimated from the available ultrasonic signals for characterizing the battery system at that time instant. Fig. 4 pictorially depicts this concept.

An AR model-based modal analysis technique can be used to determine the two unknown parameters of the vibrating system, namely: damping ratio (ζ) and natural frequency (ω_n), and the identification process is described in Section 3. In this study, the ultrasonic guided wave signals, which contain the dynamics of the Lithium-ion battery at a specific time, were modeled by the AR model. AR modeling does not require the use of the excitation signal. The AR model order $na = 2$ ($2n = 2, n = 1$) is selected, as a single degree of freedom vibrating system was assumed. BIC and RSS/SSS criteria were also employed to select the AR model order $na = 2$.

Figs. 5 and 6 show the 191 ultrasonic guided wave signals chronologically while the battery was undergoing the charging phase for path 2-1 (length direction) and path 2-3 (thickness direction), respectively. For this particular case, the battery was charged at a C-rate of C/8 following the constant current-constant voltage (CC-CV) charging protocol and discharged at a C/8 rate following the constant current discharge protocol. Ultrasonic signals are shown only for the charging phase in Figs. 5 and 6. Each ultrasonic signal was separated by 2-min time

intervals. A 5-peak tone burst actuation signal with 300 kHz center frequency was used for generating the ultrasonic signals shown in Fig. 5 while 400 kHz center frequency was used for the signals shown in Fig. 6.

In Fig. 5(a), signals are shown up to 100 μ s. It takes 15.58 μ s for the signals to travel 50 mm, that is, from sensor 2 to sensor 1. This time is referred to as the time of flight (ToF). As a result, the velocity of wave propagation for 300 kHz actuation is 3209.2 m/s. Analysis of the highest peak of the received signals reveals that as the battery undergoes charging, the amplitude and time of flight gradually decrease (Fig. 5(d)). The amplitude of the highest peak changes from 0.107 V to 0.055 V while the phase (time of flight) changes from 35.25 μ s to 34.83 μ s during charging. However, analysis of different peaks provides different values of amplitude and time of flight change. This fact is shown in Fig. 5(b) and (c), where the initial and later parts of the signals are shown, respectively. Note that in the initial part of the signal, the amplitude always decreases with charging and the magnitude of phase change is also small (the highest peak sustains 0.42 μ s change). Whereas in the later part of the signal (Fig. 5(c)), the amplitude change is not consistent, and a phase change of 0.5 μ s was observed for the peak between 55 and 57 μ s. Fig. 6 shows the ultrasonic signals obtained from path 2-3, that is, in the thickness direction. In Fig. 6(a), signals up to 110 μ s are shown and the time of flight is 5.33 μ s. Analysis of the highest peak of the received signal occurring at 24.5 μ s reveals that the signal amplitude increases from 0.267 V to 0.288 V whereas the phase changes from 24.75 μ s to 24.66 μ s (Fig. 6(d)). Note that in Fig. 6(b), which shows the initial part of the signal in the thickness direction (from 13 μ s to 20 μ s), a definite trend cannot be identified. Whereas in the later part of the signal (Fig. 6(c)), an increase in the signal amplitude with a phase change can be observed. The amplitude of the highest peak in the length direction shows an opposite trend to that of the thickness direction, however, the time of flight decreases in both cases as the battery undergoes charging.

It was mentioned in [53] that the signal envelope or the individual peaks can be correlated with the charging and discharging phase of the battery, and one may perform better than the other in different circumstances. Using the cross-wavelet transform, a smart peak selection method was also proposed which has a higher correlation with the battery charging and discharging phase. However, the proposed method in this study does not rely on any individual peaks or the signal

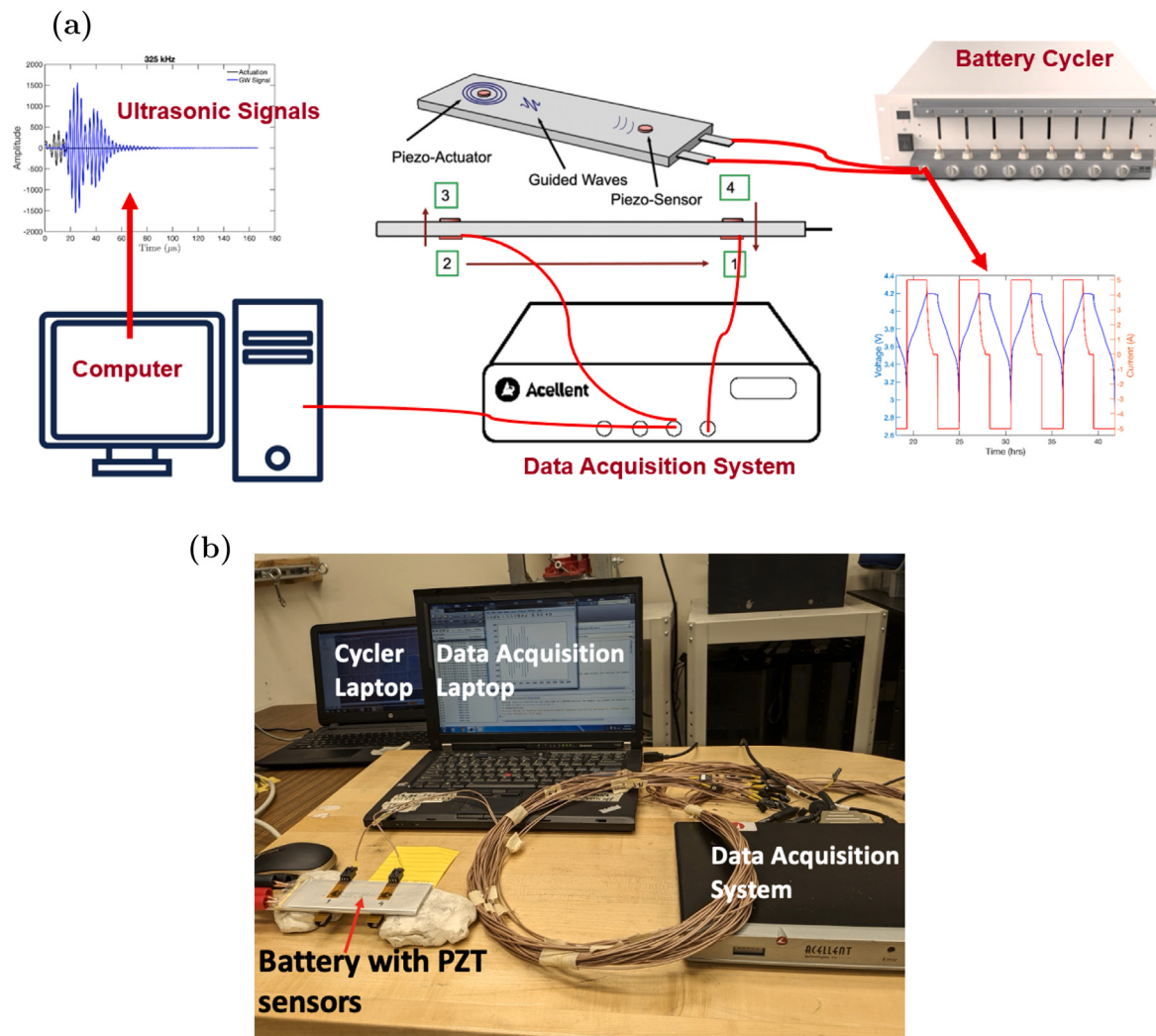


Fig. 2. (a) The schematic diagram of the battery state of charge and state of health monitoring scheme: ultrasonic signals were recorded continuously as the battery underwent the charging and discharging phase; (b) the experimental setup.

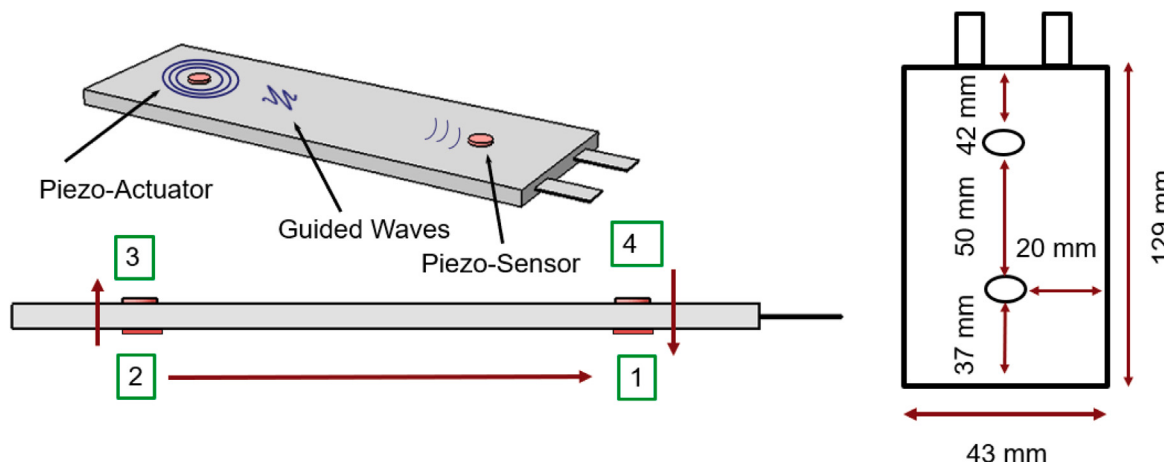


Fig. 3. Dimensions of the battery and the PZT transducer layout: the direction of the wave propagation paths are also shown.

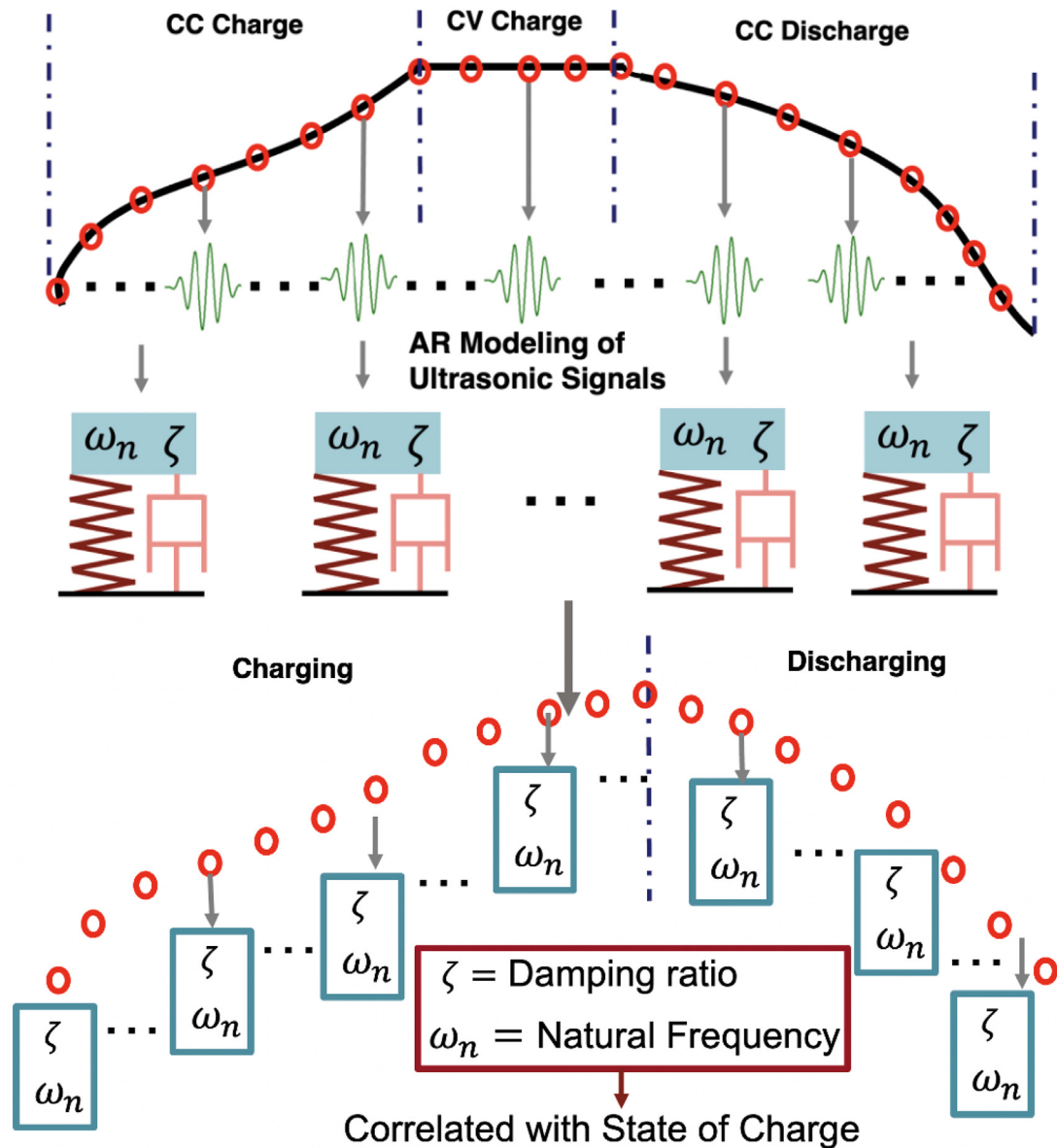


Fig. 4. The concept of battery state of charge monitoring approach using ultrasonic signals and autoregressive model-based system identification techniques. The identified natural frequency and damping ratio are correlated with the state of charge of the Lithium-ion battery.

envelope, but it uses the entire wave packet and extracts the underlying dynamics through the autoregressive (AR) modeling of the signals as explained in Section 3.

Fig. 7 shows a representative signal from the path 2-1 with 300 kHz actuation (blue line), AR(2) model-based one-step-ahead prediction of the same signal (red crossed line), and the corresponding prediction error. The residual sum of squares (RSS) over the signal sum of squares (SSS) was used as a measure of the goodness of fit. For this particular case, the percent RSS/SSS value was 0.0126. Additionally, the whiteness of the residuals was ensured by the residual sign test, which is usually carried out for model validation of the non-stationary signals. More details about the model structure selection and the model validation can be found in Refs. [49,60].

Fig. 8(a) and (b) show the correlation between the two model parameters α_1 and α_2 of the AR(2) model for the 191 ultrasonic signals as the battery undergoes charging phase. In Fig. 8(a), the evolution of the model parameters is shown for 275 kHz actuation frequency for

path 2-1 (length direction). Note that at the beginning of time, or at the start of the charging phase, the parameters are located on the upper side of the plot. As time progresses, and the state of charge increases, the parameters evolve to move on the lower side of the plot. Similarly, Fig. 8(b) shows the evolution of the parameters for 400 KHz actuation for path 2-3 (thickness direction) and the parameters move from left to right. As a result, by following the evolution of the two parameters extracted from the entire waveform of the received signal, it is possible to keep track of the state of charge. With this approach, the tracking of the individual peaks of the ultrasonic signals for correlating with the state of charge is not necessary.

5.1. State of charge characterization

The natural frequencies were estimated from the ultrasonic signals propagated in the length direction of the battery (path 2-1), which were generated and captured with the help of the permanently installed

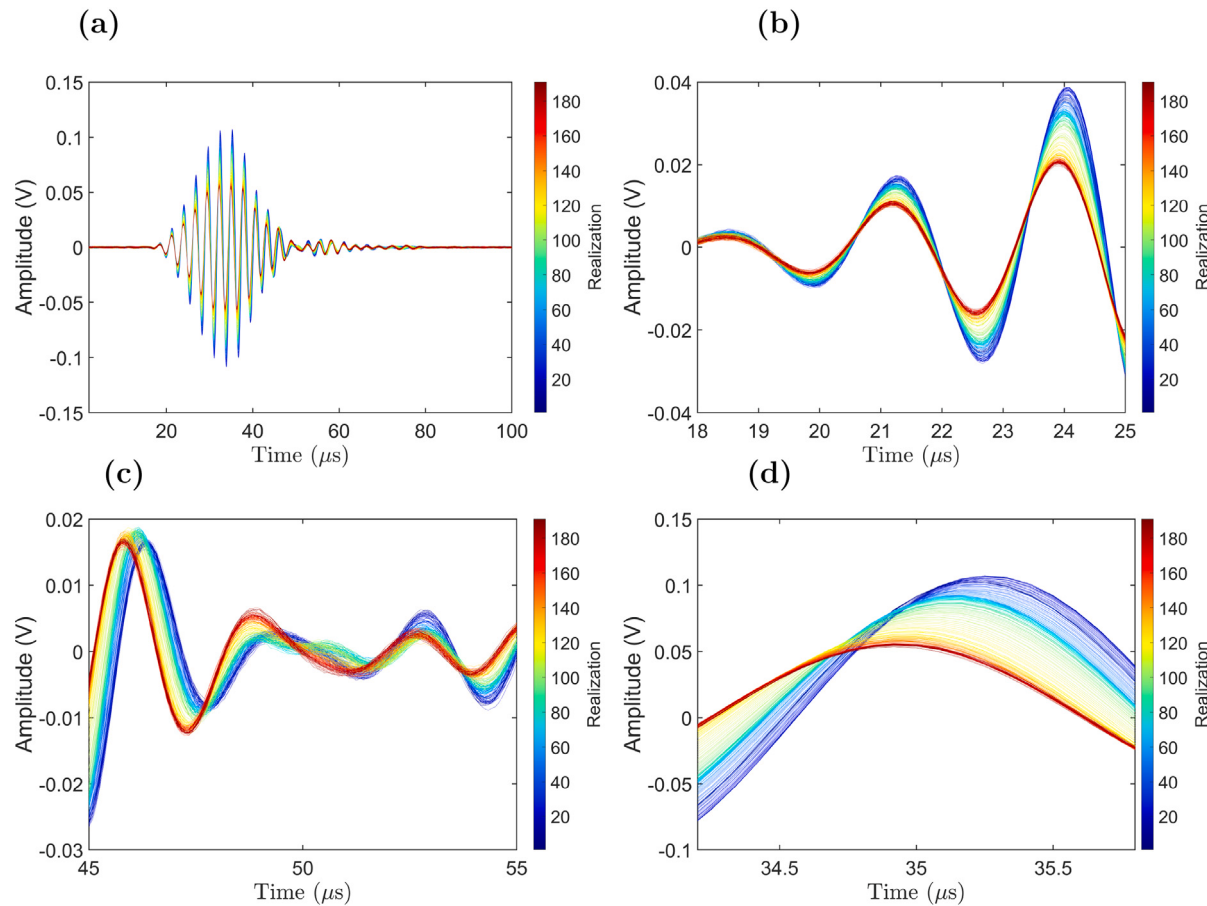


Fig. 5. Waveform of the 191 ultrasonic signals for path 2-1 (length direction) as the battery was undergoing charging phase with the actuation frequency of 275 kHz: (a) the entire 100 μ s of signals; (b) the zoomed-in view of the initial part of the signals; (c) the zoomed-in view of the later part of the signals; (d) the zoomed-in view of the middle part of the signals. The red color in the color bar signifies that the signals are at the later part of the charging phase.

piezoelectric transducers. It was hypothesized that each ultrasonic signal, which is approximately 120 μ s long, represents a spring mass damper vibrating system at a specific time instant during the charging and discharging phase of the battery. An AR(2) model was used to model this hypothetical single-degree-of-freedom vibrating system. Thus the underlying dynamics of the ultrasonic signals are related to the two modal parameters: natural frequency and damping ratio. These modal parameters can be estimated from Eq. (12) and by following the process described in Section 3.

Fig. 9(a) and (b) show the voltage and current profile with time. The voltage gradually increased to 4.2 V in 1.1 h, where a C/2 constant current charging protocol was applied. After that, a constant voltage charging protocol was applied with a cutoff current of C/40. After that, a 5-min rest was applied. The battery was discharged with C/2 constant-current discharge protocol until 3.0 V. **Fig. 9(c)** and **Fig. 9(d)** can be explained with reference to **Fig. 9(a)**. Note that initially, up to 0.2 h, the damping ratio ζ and natural frequency ω_n slightly decreases and increases, respectively. From 0.2 h to 1.2 h, where the constant current charging protocol was applied, the damping ratio increased from 0.008 to 0.02 and the natural frequency decreased from 3.374e5 Hz to 3.243e5 Hz. From 1.2 h to 1.94 h, where a constant voltage charging scheme was applied, the damping ratio increased from 0.02 to 0.08 and the natural frequency decreased from 3.243e5 Hz to 2.484e5 Hz. Note that the rate of increase of the damping ratio and the decrease of the natural frequency is higher in the constant voltage charging scheme than in the constant current charging scheme.

From 2 to 3.3 h, the battery undergoes constant current discharge protocol (C/2 rate). The damping ratio decreased from 0.08 to 0.005 and the natural frequency increased from 2.484e5 Hz to 3.245e5 Hz in the discharge phase.

Fig. 10 shows the evolution of damping ratios and natural frequencies for C/8 constant current charging and discharging rate. In **Fig. 10(a)**, the constant current charging at C/8 rate occurs until 7.9 h to reach 4.2 V. From 7.9 h to 8.2 h, the constant voltage charging occurs with a cutoff current of C/40. From 8.28 h to 16.6 h, the constant current discharge occurs with a C/8 rate until 3.0 V. The damping ratio and natural frequency obtained from the AR modeling of the 478 ultrasonic signals excited by a 5-peak tone burst signal with a center frequency of 300 kHz are shown in **Fig. 10(c)** and (d). **Fig. 10(c)** shows the increase and decrease in the damping ratio with the charging and discharging phase of the battery, respectively. Note that from the start to 0.42 h of charging, an initial decrease in the damping ratio from 0.015 to 0.013 can be observed. From 0.42 h to 8.2 h, the increase in damping ratio occurs in three stages. In the first stage, the damping ratio increases at a slow rate from 0.42 h to 3.38 h (damping ratio increased from 0.013 to 0.021). In the second stage, the damping ratio increases at an intermediate rate from 3.38 h to 7 h (damping ratio increased from 0.021 to 0.047). And, finally, in the third stage, the damping ratio increases at a faster rate from 7 h to 8.2 h (damping ratio increased from 0.046 to 0.09). **Fig. 10(d)** shows the decrease and increase of the natural frequency (exact opposite trend of damping ratio)) with the charging and discharging of the battery, respectively. Note that the decrease in natural frequency also occurs in different

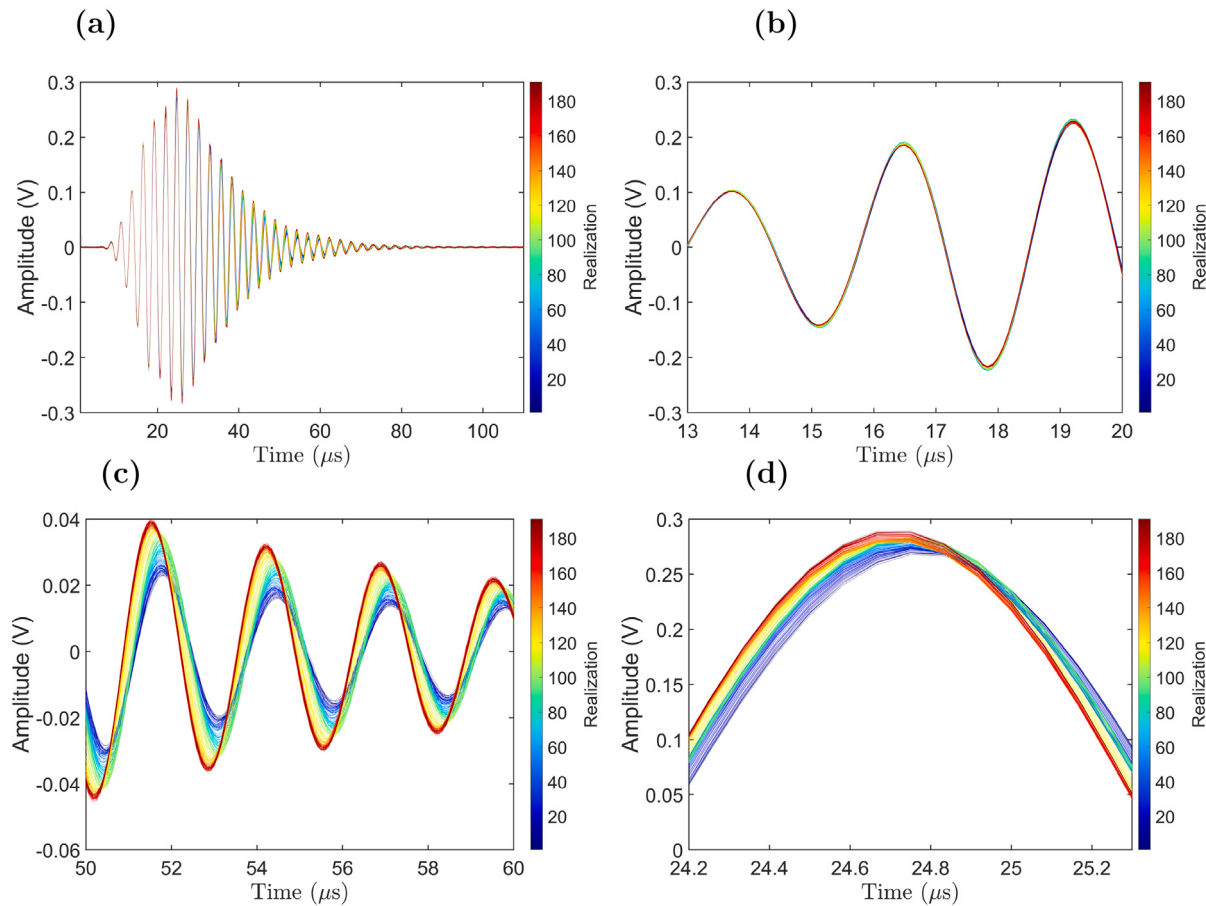


Fig. 6. Waveform of the 191 ultrasonic signals for path 2-3 (thickness direction) as the battery was undergoing charging phase with the actuation frequency of 400 kHz: (a) the entire 110 μ s of signals; (b) the zoomed-in view of the initial part of the signals; (c) the zoomed-in view of the later part of the signals; (d) the zoomed-in view of the middle part of the signals. The red color in the color bar signifies that the signals are at the later part of the charging phase.

stages, and the rate of decrease is different for different stages. Overall, the natural frequency decreases from 3.277×10^5 Hz to 2.382×10^5 Hz during charging and increases again during the discharge phase.

Fig. 11 shows how the natural frequencies change with time as the Lithium-ion battery undergoes the charging and discharging phases at four different C-rates, namely: C/2, C/3, C/8, and C/10. The state of charge obtained from the battery cycler was also plotted to observe the correlation between the state of charge and the change in natural frequencies. The state of charge was obtained as the ratio of the current capacity to the maximum capacity within a single cycle. Note that as the state of charge increases, the natural frequency gradually decreases (apart from the start of the charging phase). For C/2 and C/3 charging rates, the decrease in natural frequency with the increase in the state of charge tends to be nonlinear, however, with the slower charging and discharging rate (C/10), the correlation tends to be linear. Similarly, in Fig. 12, the correlation between the damping ratio and the state of charge is shown for different C-rates. Note that for the damping ratio, an exact opposite trend to that of the natural frequency can be observed, that is, the damping ratio increases with the increase in the state of charge. The correlation becomes more and more linear as slow charging and discharging rate was used (C/10 rate).

Figs. 13 and 14 show the natural frequency and the damping ratio, respectively, for different C-rates. The state of charge was also plotted for both cases. In this case, the ultrasonic signals were received in the thickness direction of the battery, that is, path 2-3. A 5-peak tone burst actuation with a center frequency of 400 kHz was used. Note

that for the thickness direction, the natural frequency increases with the increase in the state of charge. Additionally, the damping ratio decreases with the increase in the state of charge, and the evolution appears to be noisy (Fig. 14). This is the exact opposite phenomenon compared to the length direction of the battery, that is, for path 2-1. Also, note that the change in the damping ratios is small in the thickness direction (1.8×10^{-3} to 2.6×10^{-3} for C/10 charging and discharging rate) compared to the length direction. For the discharge phase of the battery, the decrease in the natural frequency with the decrease in the state of charge occurs in a linear fashion as slower discharge rates are used (C/3, C/8, and C/10 rates).

5.2. State of health characterization

In order to characterize the state of health of Lithium-ion batteries with ultrasonic signals, 5 pouch cell Lithium-ion batteries with 10 Ah nominal capacity were continually charged and discharged up to 100 cycles. The maximum and minimum voltage of the batteries were 3.0 V and 4.2 V, respectively. One complete cycle underwent the following 4 stages: (i) constant current charging, (ii) constant voltage charging, (iii) rest, and constant current discharge. Ultrasonic signals were simultaneously collected every 5-min intervals. Similar to the case of state-of-charge characterization, 16 different actuation frequencies were considered for generating the ultrasonic signals. 118,400 ultrasonic signals were collected over the span of 500 h, resulting in 26 GB (GB) of data. Once the ultrasonic signals were collected, time

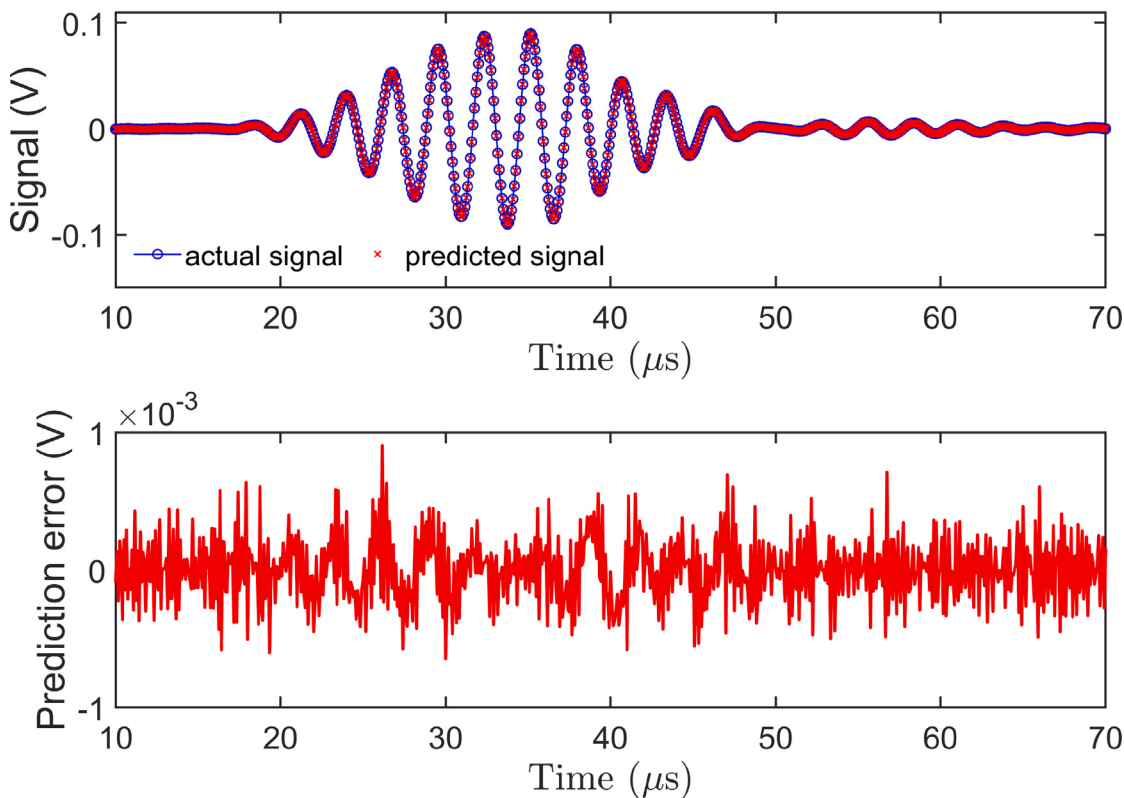


Fig. 7. AR(2) model-based one-step-ahead prediction and the prediction error for a representative ultrasonic signal.

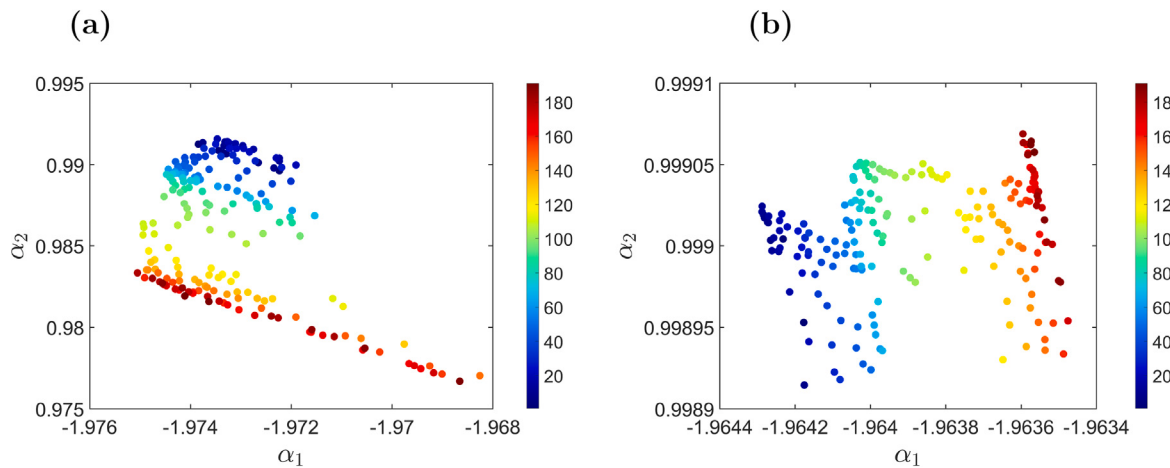


Fig. 8. The correlation of the AR(2) model parameters α_1 and α_2 obtained from the AR modeling of the ultrasonic signals: (a) evolution of the model parameters for the signals excited at 275 kHz and path 2-1 (length direction); (b) evolution of the model parameters for the signals excited at 400 kHz and path 2-3 (thickness direction). The red color in the color bar indicates that the signals are at the later part of the charging phase.

series-based autoregressive (AR) modeling of the signals was performed following the process outlined in Section 3 to extract the two dynamic parameters (natural frequency and damping ratio) from each ultrasonic signal.

Fig. 15(a) shows the plot of 7400 natural frequencies (each dot) extracted from the 7400 ultrasonic signals excited by a 5-peak tone burst signal with 225 kHz actuation center frequency. To complete 100

cycles of the battery, 500 h were required. Note that the peak values of the frequencies decrease with time. This decrease in the peak values is correlated with the state of health of lithium-ion batteries. In order to facilitate the extraction of the peak values, an envelope was formed by performing the Hilbert transform of the natural frequencies. In this case, the array of natural frequencies is considered as a signal. The filter length used was 16 data points. This is shown in Fig. 15(b). In

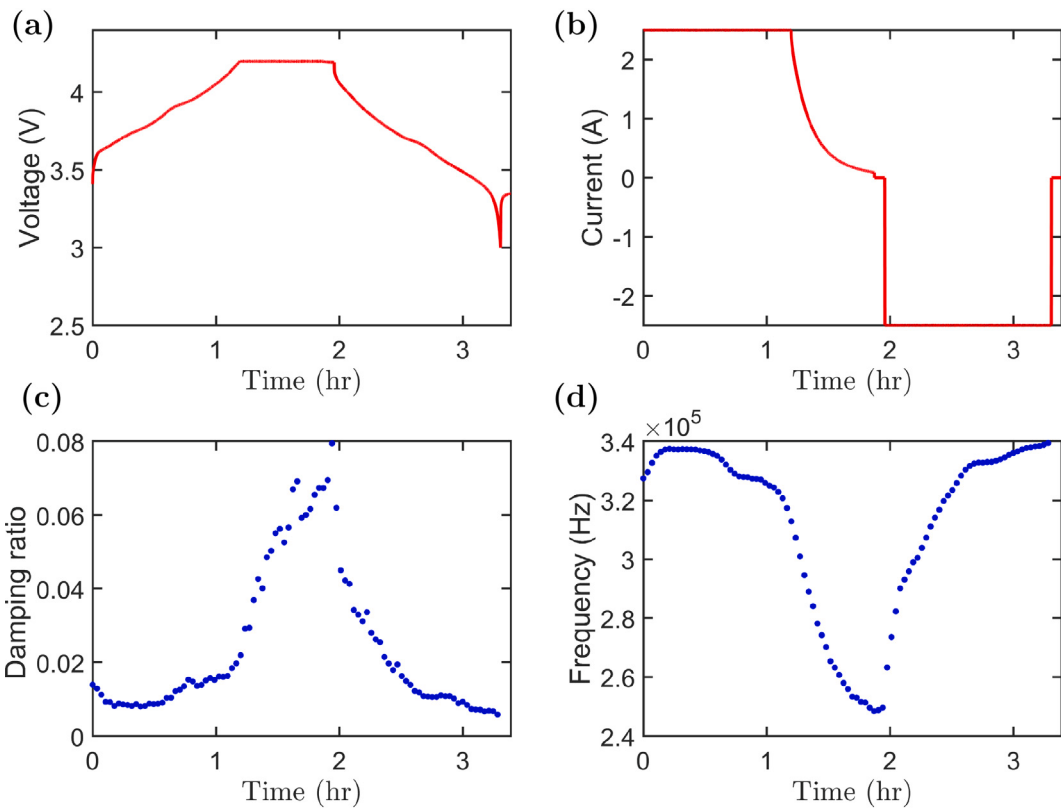


Fig. 9. The voltage and current profile of the battery for C/2 constant current charge and discharge rate for a single cycle and the associated change in the damping ratio and natural frequency. The damping ratios and the natural frequencies are extracted from the ultrasonic signals in the length direction of the battery.

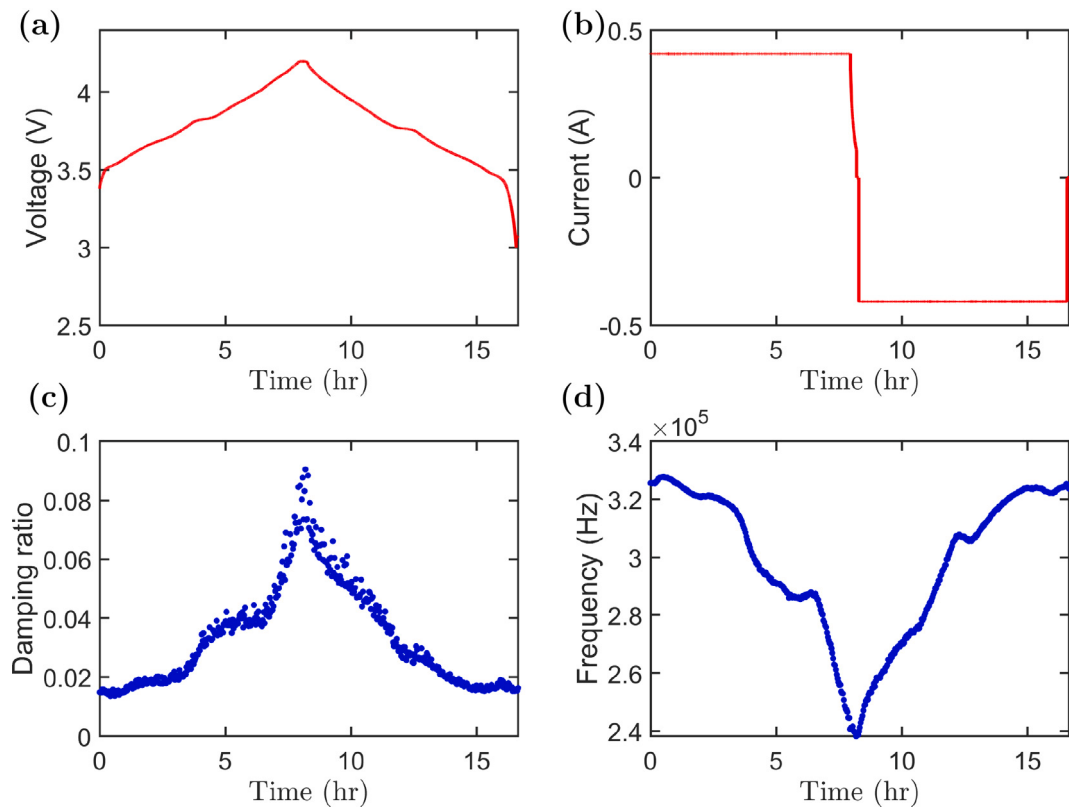


Fig. 10. The voltage and current profile of the battery for C/8 constant current charge and discharge rate for a single cycle and the associated change in the damping ratio and natural frequency. The damping ratios and the natural frequencies are extracted from the ultrasonic signals in the length direction of the battery.

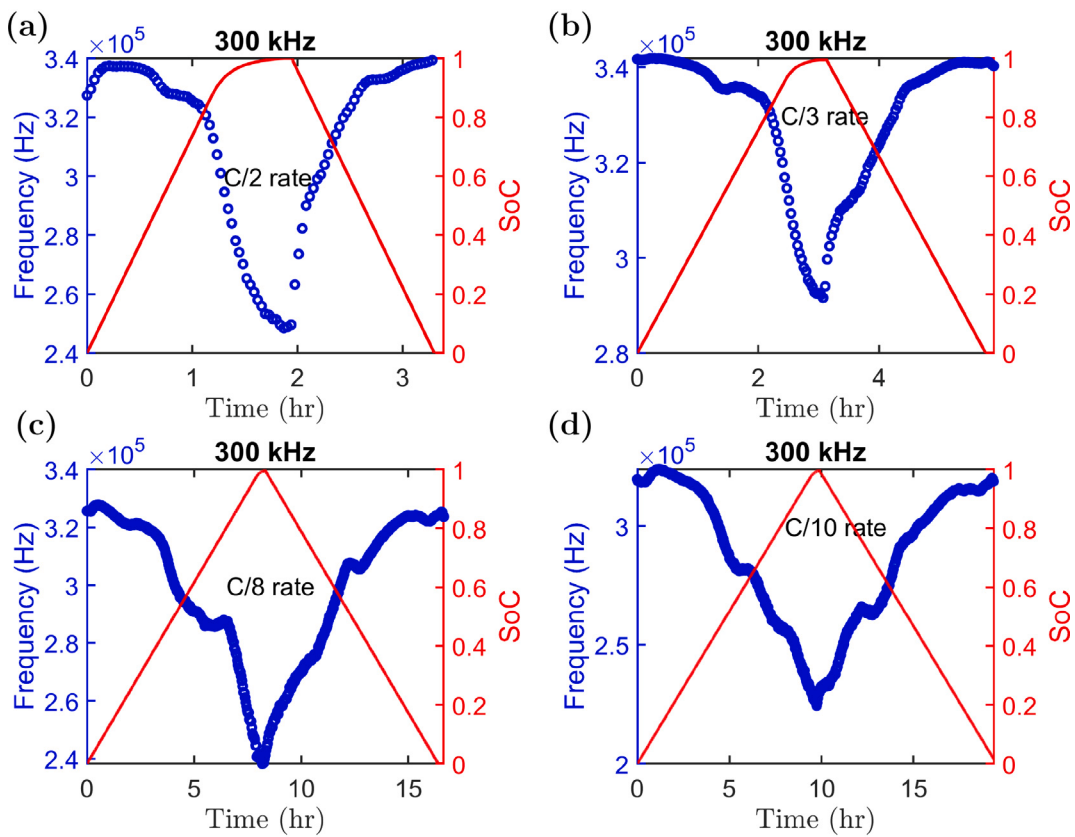


Fig. 11. Natural frequencies obtained from the AR-modeling of the ultrasonic signals excited by the 5-peak tone burst actuation signal with 300 kHz center frequency and the state of charge obtained from the battery cycler for different C-rates (for path 2-1, that is, in the length direction): (a) C/2; (b) C/3; (c) C/8; (d) C/10.

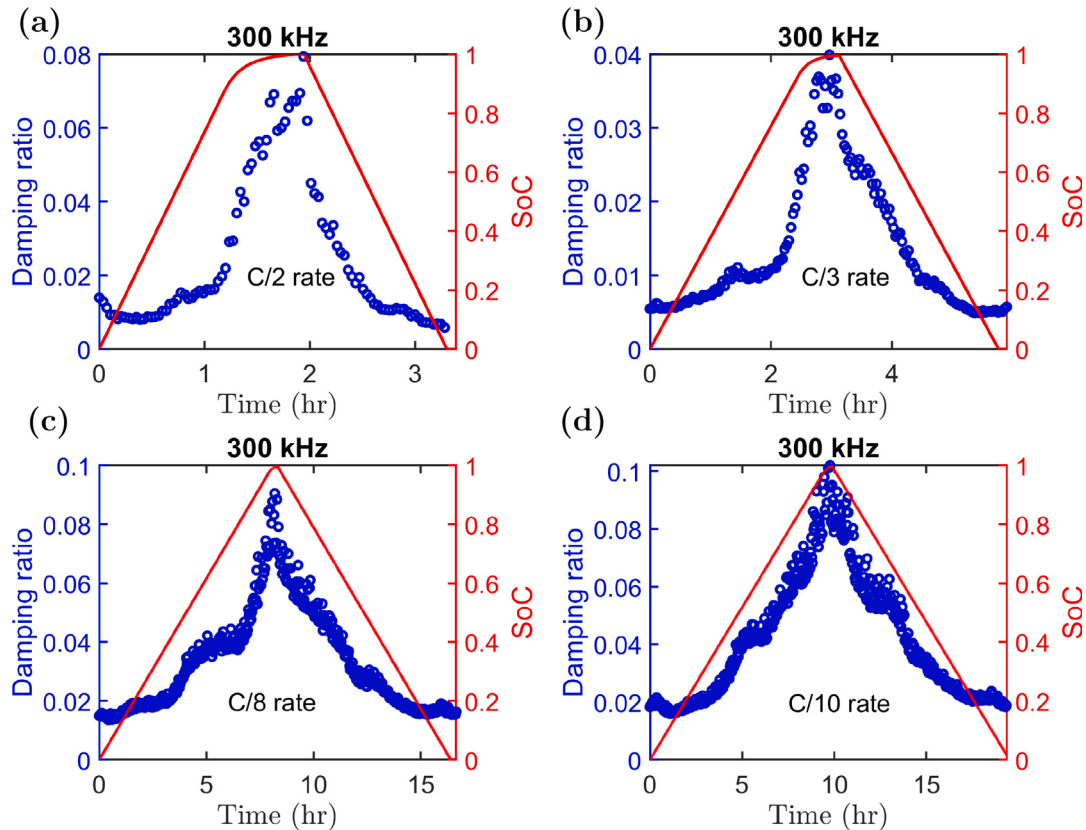


Fig. 12. Damping ratio obtained from the AR-modeling of the ultrasonic signals excited by the 5-peak tone burst actuation signal with 300 kHz center frequency and the state of charge obtained from the battery cycler for different C-rates (for path 2-1, that is, in the length direction): (a) C/2; (b) C/3; (c) C/8; (d) C/10.

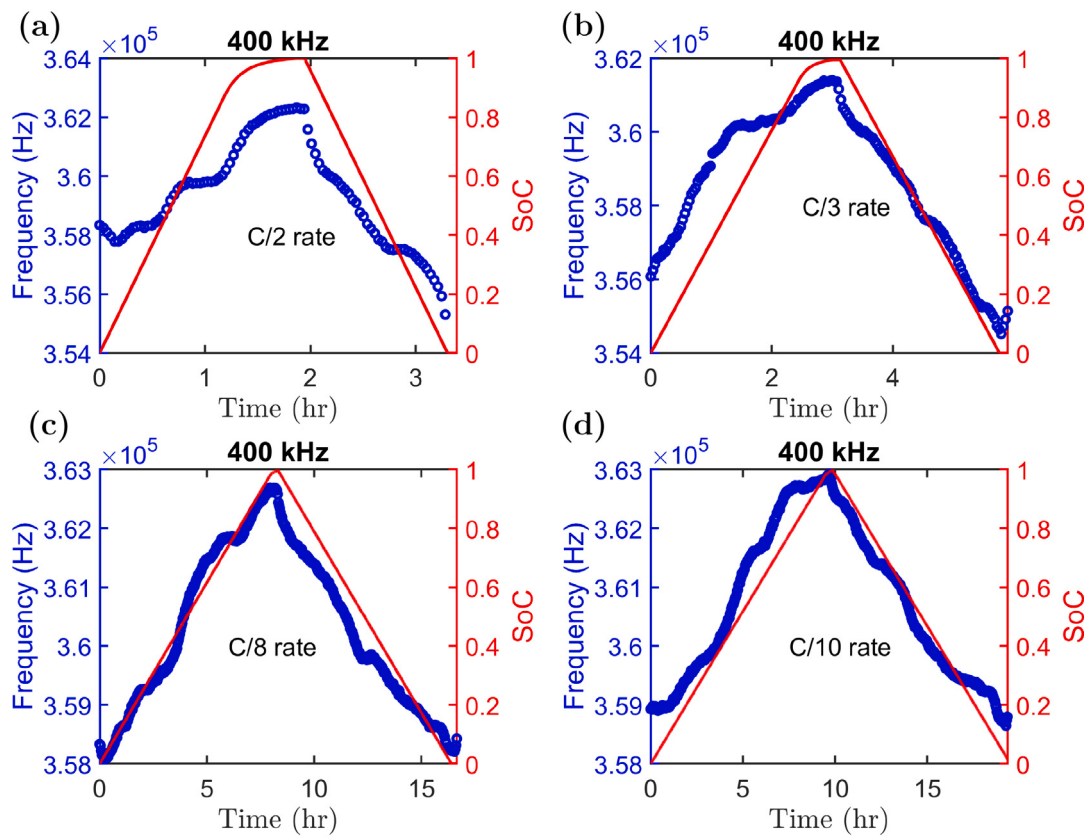


Fig. 13. Natural frequencies obtained from the AR-modeling of the ultrasonic signals (in the thickness direction of the battery, that is, path 2-3) excited by the 5-peak tone burst actuation signal with 400 kHz center frequency and the state of charge simultaneously obtained from the battery cycler for different C-rates: (a) C/2; (b) C/3; (c) C/8; (d) C/10.

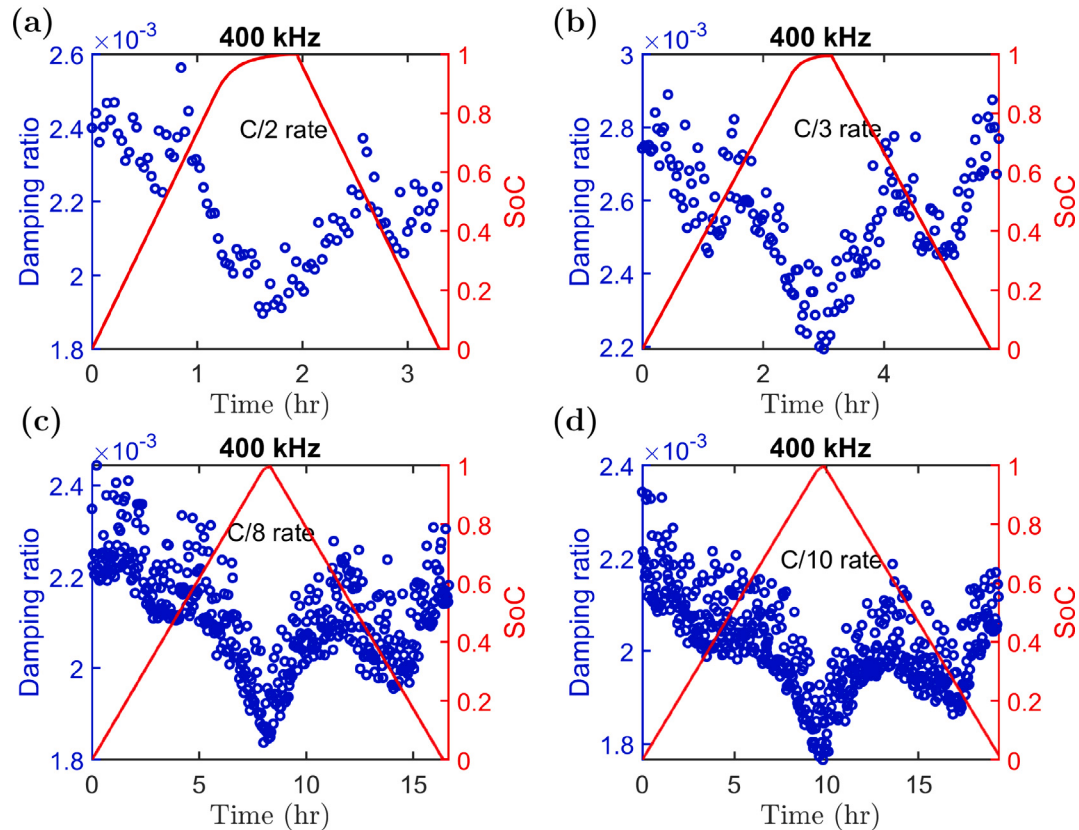


Fig. 14. Damping ratios obtained from the AR-modeling of the ultrasonic signals (in the thickness direction of the battery, that is, path 2-3) excited by the 5-peak tone burst actuation signal with 400 kHz center frequency and the state of charge simultaneously obtained from the battery cycler for different C-rates: (a) C/2; (b) C/3; (c) C/8; (d) C/10.

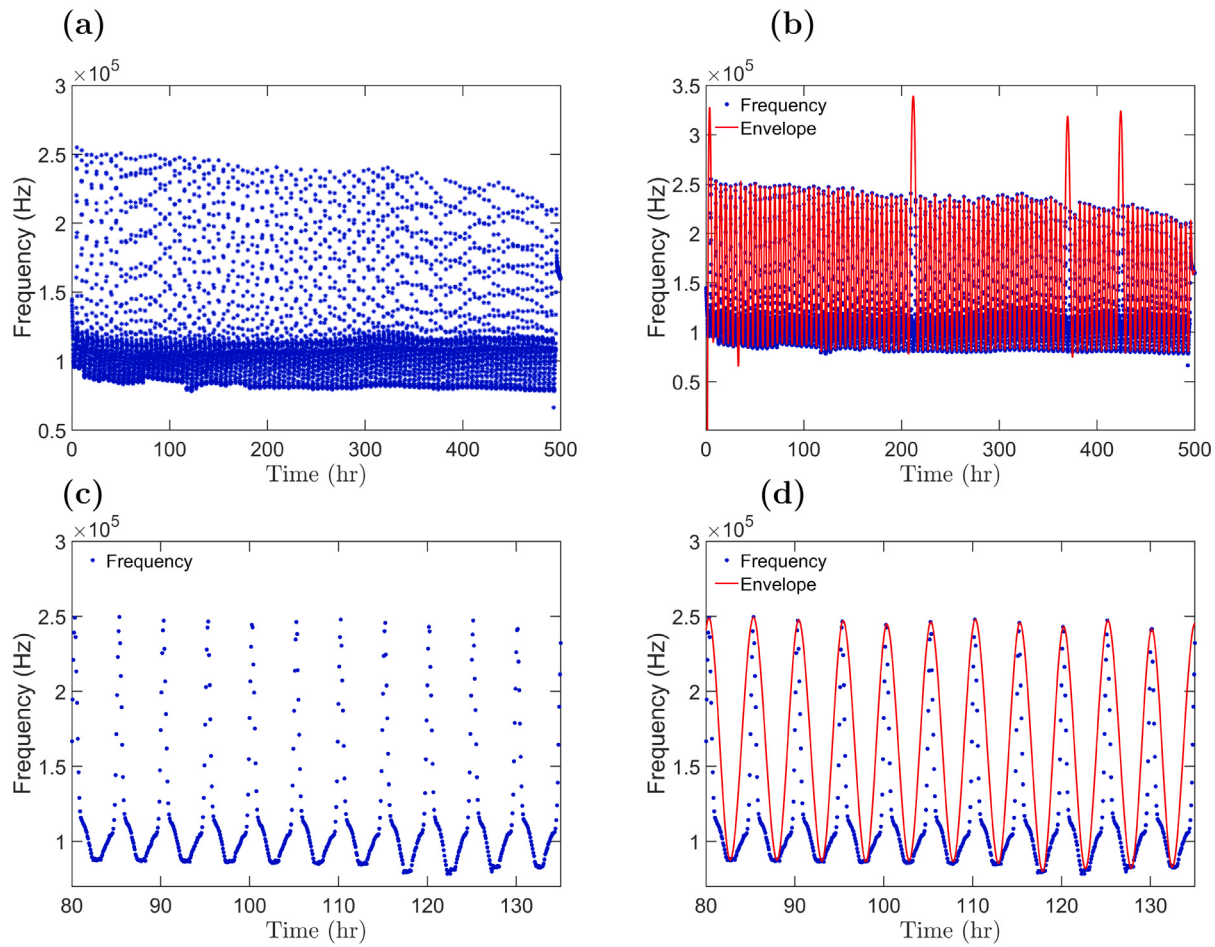


Fig. 15. (a) Natural frequencies extracted from the ultrasonic signals for 100 cycles: the peak values of the frequencies show a gradually decreasing trend; (b) natural frequency and the envelope plotted together; (c) zoomed-in view of (a); zoomed-in view of (b).

Fig. 15(c), note that natural frequencies get as high as 2.5 kHz during fully charged state and as low as 1 kHz during fully discharged state.

Fig. 15(d) is the zoomed-in view of **Fig. 15(b)**.

Fig. 16 provides more insight into the selection of peaks. **Fig. 16(a)** shows natural frequencies only for two cycles and the associated envelope obtained from the Hilbert transform. Note that region A, C, and D have local maxima or minima, and can also be used to establish correlations with the state of health of lithium-ion batteries. However, in this study only region B was considered. During the extraction of the peaks in region B with Hilbert transform, artifacts may occur and care should be taken to avoid this. This phenomenon is shown in **Fig. 16(b)**. Note that at 210 and 215 h, two individual cycles exist, however, the envelope shows only one cycle and one peak.

In **Fig. 17(a)**, a direct correlation was obtained between the peaks of the extracted natural frequencies and the state of health of lithium-ion batteries. The state of health was estimated by directly obtaining the capacity at each cycle from the battery cycler and dividing the current capacity by the nominal capacity of the battery. Note that as the cycle number increases, the state of health gradually decreases. With 100th cycle, the state of health decreased about 1 percent. And the peaks from the natural frequencies (red dots) independently obtained from the ultrasonic signals follow the decreasing trend of the battery state of health. However, for damping ratios (**Fig. 17(b)**), an increasing trend can be observed as the battery state of health decreases. As a result, when the battery capacity data is not directly available from the battery cycler, which is often the case in any in-service conditions, by collecting and analyzing the ultrasonic data and extracting meaningful information such as natural frequencies and damping ratios, it is possible to

have information about the battery degradation and battery state of health.

6. Discussions

In general, a battery can be considered as a multi-degree-of-freedom vibrating system having a system of masses, springs, and dampers. This system can be forced to vibrate with the application of an external excitation. The response of the forced excitation can be measured experimentally and a frequency response function can be obtained. If the system gets changed somehow, that change would be manifested as a change in its frequency response function. In structural mechanics, this change in the system can occur in the form of damage, degradation, formation of cracks etc. For battery, the change can occur in the form of electrode degradation, electrode cracking, change in modulus and density of the electrode due to the charge and discharge process of the battery. Thus, by analyzing only the frequency response function obtained from the battery system at different state, the inverse estimation and inference of the battery state of charge, battery state of health, and battery degradation can be obtained. As the battery undergoes the charge or discharge state, a shift in the resonant frequencies or natural frequencies can be observed [58,59,61].

However, the vibration test of the battery to acquire the frequency response function requires sophisticated and precise instrumentation and may be difficult to implement during in-service operations for online and automated monitoring of the battery. Additionally, the location of the driving point of the piezoelectric disk actuator directly affects the frequency response function of the battery cell as it dictates

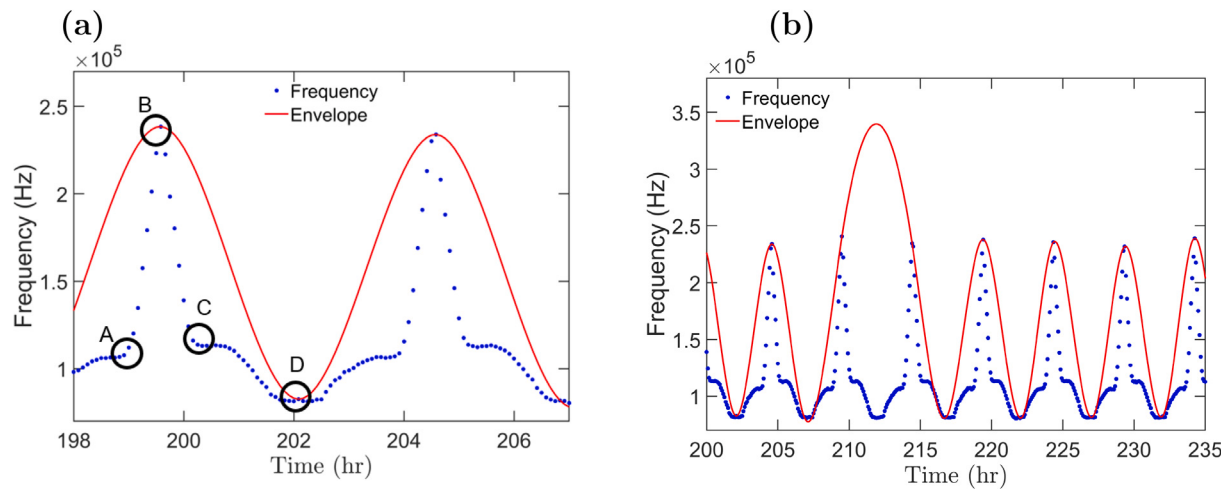


Fig. 16. (a) Natural frequencies and the corresponding envelope for only two cycles which clearly show how the frequencies change during the charge and discharge of the battery; (b) artifact created by the envelope at 210 and 215 h.

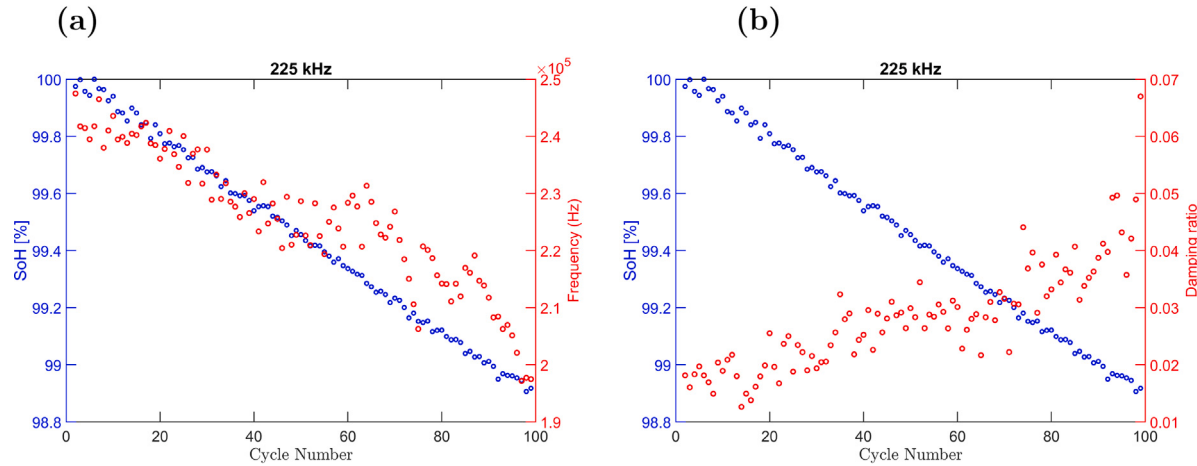


Fig. 17. (a) Battery capacity expressed in terms of the state of health (SoH) for 100 cycles from the battery cycler and the peak values of the natural frequencies extracted from the ultrasonic signals: both quantities show a gradual decreasing trend as the battery undergoes cycling; (b) battery SoH and the damping ratio plotted together, the damping ratio increases as the SoH decreases over 100 cycles.

how the battery will vibrate. Waiting time on the order of at least 6 h is required before a new measurement of the frequency response function can be taken to minimize the effect of drift on the test results. In this study, the above-mentioned difficulties are resolved by utilizing ultrasonic guided wave signals for measuring the state of charge and the state of health of the battery.

In this study, four piezoelectric transducers were permanently installed on the battery. The circular-shaped piezoelectric transducers had a diameter of 6.35 mm and constitute only a small portion of the battery. The piezoelectric transducers can be excited with an external excitation pulse generating ultrasonic waves. The generated ultrasonic waves propagate in all directions and are received by the other piezoelectric transducers. During propagation, the ultrasonic waves interact with the anode and cathode materials and contain information about any change such as the elastic modulus and density change of the same. As a result, the permanently installed piezoelectric transducers vibrate the battery with high frequency (usually 150–700 kHz) in the form of propagating waves. The response signal obtained from the vibration test of the battery, which is used to obtain the frequency response function, is analogous to the propagating ultrasonic guided waves. Ultrasonic signals can be excited and collected at any time without the need for any additional wait time. In this study, ultrasonic signals were collected at two-min intervals as the battery underwent the charge and

discharge process. This gives a better resolution to capture the charging and the discharging process with ultrasonic waves.

In this study, an autoregressive model-based modal analysis technique was applied on the response ultrasonic guided wave signals to extract the natural frequency and damping ratio of the battery system. Fig. 7 indicates that batteries can be modeled as a single-degree-of-freedom vibrating system instead of a multi-degree-of-freedom vibrating system. This is because the AR model order $na = 2$ is sufficient to achieve a low RSS/SSS value. This simplifies the analysis and a direct correlation between the state of charge and the extracted natural frequencies and damping ratios can be established. Figs. 9 to 14 shows the relationship among the voltage, current, state of charge, and the two extracted parameters from the ultrasonic signals, namely: the natural frequency and the damping ratio. The effect of C-rate and the propagation direction of the wave on the extracted parameters were also investigated. In Fig. 11, for the length direction signals, the extracted natural frequencies decrease as the state of charge increases. On the other hand, in Fig. 13, for the thickness direction signals, a quite opposite trend can be observed, that is, the natural frequencies increase with the increase in the state of charge. This phenomenon can be explained in terms of the following equation:

$$\omega_n = \sqrt{\frac{k}{m}} \quad (22)$$

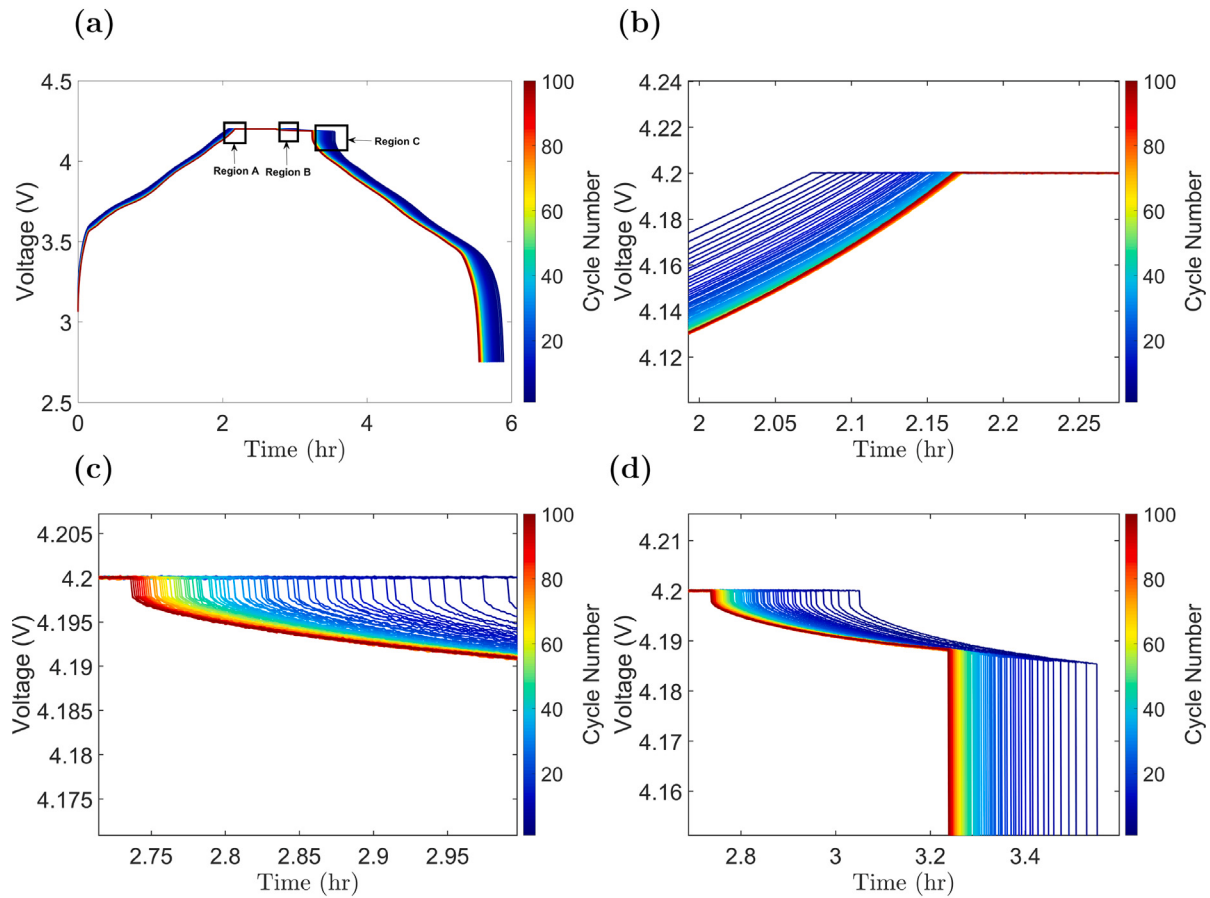


Fig. 18. The voltage profile of the battery for 100 cycles: (a) shows the voltage profile for constant current charging, constant voltage charging, rest, and the constant current discharge and how they change over 100 cycles; (b) zoomed-in view of region A; (c) zoomed-in view of region B; (d) zoomed-in view of region C.

In Eq. (22), ω_n is the natural frequency, k is the stiffness and m is the mass of the cell. The stiffness k is proportional to the elastic modulus (Young's modulus). The cells used in this study have NMC cathode and graphite anode. During charging, delithiation of the cathode and lithiation of the anode occurs. It was reported that during delithiation of the cathode and with the increase in the state of charge, the Young's modulus monotonously decreases from 142.5 GPa to 111.6 Gpa [62]. On the other hand, for graphite anode, the change in Young's modulus is direction sensitive. The planar Young's moduli for graphite and LiC_6 are 974.93 and 877.35 GPa, respectively [63]. As a result, there is a net decrease in the Young's modulus in the planar or length direction during charging of the battery. This explains the decrease in the natural frequencies with the increase in the state of charge in the length direction. In the c -axis direction or in the thickness direction of the battery, the Young's modulus of graphite and LiC_6 are 11.38 and 52.11 GPa. As a result, there is a net increase in the Young's modulus in the thickness direction. This is why the natural frequencies increase with the increase in the state of charge in the thickness direction. The damping ratios are inversely proportional to the natural frequencies as can be observed from Eq. (4). This explains the trend for damping ratios in Figs. 12 and 14.

Figs. 15 to 17 deals with the determination of the state of health of lithium-ion batteries using ultrasonic signals. Fig. 17 establishes a correlation between the state of health and a decreasing trend of the natural frequencies and an increasing trend of damping ratios. In this case, the signals were collected in the length direction. It was reported that with the increase in the cycle number, the Young's modulus of the NMC cathode gradually decreases [62]. Similarly, with the increase in the cycle number, Young's modulus monotonically decreases in the

graphite anode [64]. The change in these mechanical properties in the anode and cathode materials explains the decreasing trend of natural frequencies and increasing trend in damping ratios with the increase in cycle number. As a result, by using ultrasonic waves it is possible to probe the real-time state of health of the battery.

It is to be mentioned here that at higher C-rates, lithium-ions have to move faster during charging and discharging and may have little time to settle down. As a result, the mechanical property change may not be uniform or gradual, which may be reflected in the wave propagation signals. For the length direction signals, there is non-linearity in the low SoC for the extracted parameters, which may provide poor correlation. However, for the discharge case, and in the thickness direction signals, the change was found to be gradual even in low SoC or high SoC. As a result, in order to achieve optimal performance, information from the thickness direction as well as from the length direction should be considered.

7. Conclusions

In this study, ultrasonic guided wave signals, generated and received by permanently installed piezo-electric transducers, were used to monitor the state of charge and state of health of the battery. The lithium-ion battery was considered as a single-degree-of-freedom vibrating system, and the received ultrasonic signals as the response from the system. From the class of stationary stochastic time series models, an output-only autoregressive model was employed to model the underlying dynamics of the propagating ultrasonic waves, thus extracting the two modal parameters of the single-degree-of-freedom vibrating system, namely: the natural frequency and damping ratio. This approach removes some of the difficulties encountered in the

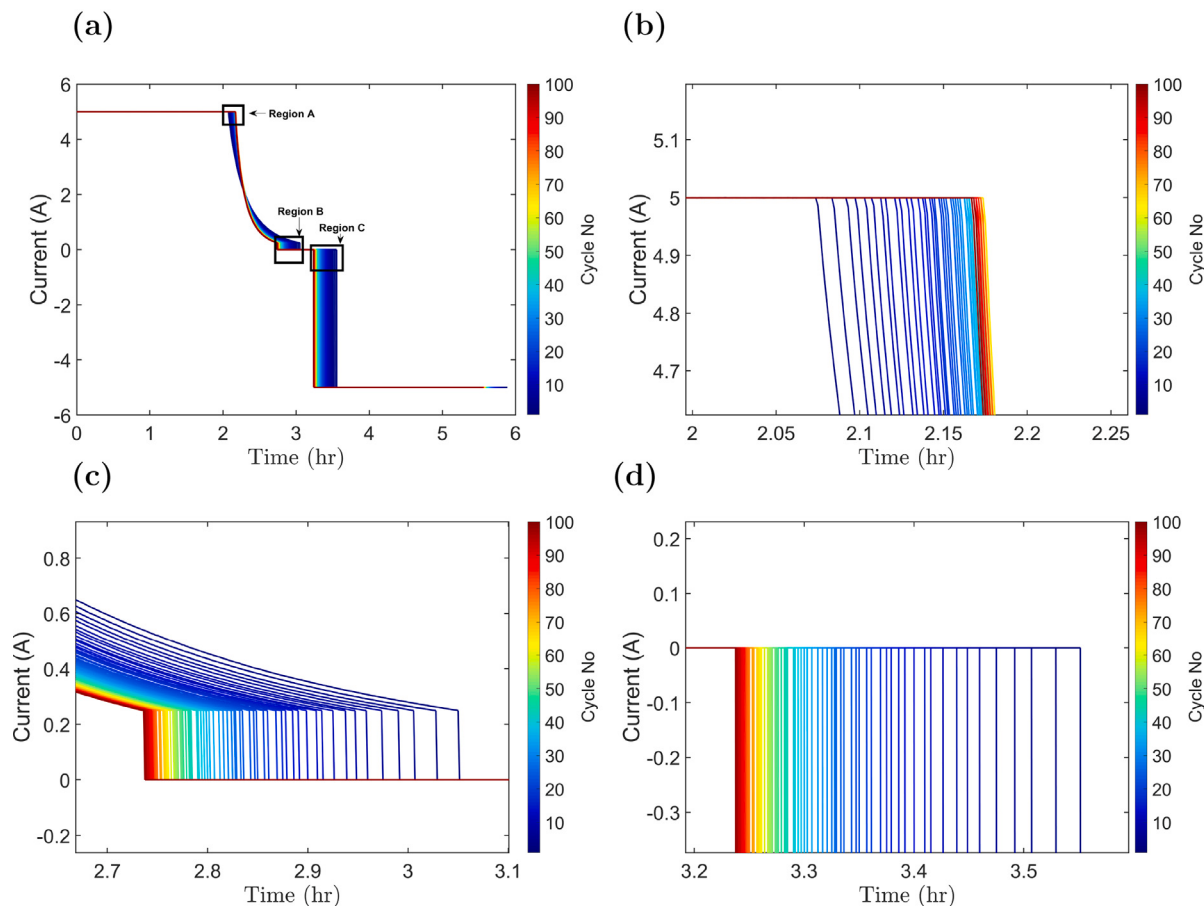


Fig. 19. The current profile of the battery for 100 cycles: (a) shows the current profile for constant current charging, constant voltage charging, rest, and the constant current discharge and how they change over 100 cycles; (b) zoomed-in view of region A; (c) zoomed-in view of region B; (d) zoomed-in view of region C.

vibration test of the lithium-ion batteries, such as the repeatability and resolution, where the frequency response function is typically used to extract the system parameters. Vibration tests of the battery are usually performed in the lower frequency regime (10–1000 Hz), and thus may not be sensitive enough to detect the minor changes in the electrode materials of the battery. On the other hand, ultrasonic signals are actuated in the kilo Hertz (kHz) to mega Hertz (MHz) frequencies, thus having the capability to interact with minor changes in the electrode materials.

In this study, ultrasonic signals were actuated and received continuously as the battery underwent the charge and discharge phase. The change in natural frequencies and damping ratios were directly correlated with the state of charge and the state of health of the battery. This change was due to the overall increase or decrease of Young's modulus of the electrode materials of the battery. The change in Young's modulus of the graphite due to lithiation or delithiation in the thickness direction and in the longitudinal direction has different magnitudes, which subsequently affects the increase or decrease of the natural frequency and damping ratio. For the state of health of the battery, the gradual decrease in the natural frequency with the cycle number implies an overall decrease in Young's modulus of the electrode materials. The generation and reception of the ultrasonic waves with the help of the permanently installed piezoelectric transducers is simple and easy to automate. Thus the presented approach is suitable for the estimation of the state of charge and state of health of the lithium-ion battery during service in an automated way.

Although the presented approach was shown for the case of lithium-ion batteries, however, it may also be applicable to solid state, sodium ion, and other types of battery systems. As a future research effort, the effect of temperature, expansion, and abusive conditions can be

investigated. The high-frequency ultrasonic signals are susceptible to noise and other environmental effects, which may influence the estimation of natural frequency and damping ratio, subsequently affecting the correlation between the state of charge and the state of health, which also needs to be investigated.

CRediT authorship contribution statement

Shabbir Ahmed: Writing – review & editing, Writing – original draft, Methodology, Investigation, Formal analysis, Data curation, Conceptualization. **Saman Farhangdoust:** Writing – review & editing, Resources, Methodology. **Fu-Kuo Chang:** Writing – review & editing, Supervision, Resources, Funding acquisition.

Declaration of competing interest

The authors declare the following financial interests/personal relationships which may be considered as potential competing interests: Fu-Kuo Chang reports financial support was provided by Advanced Research Projects Agency-Energy. If there are other authors, they declare that they have no known competing financial interests or personal relationships that could have appeared to influence the work reported in this paper.

Acknowledgments

The work is supported by the Advanced Research Projects Agency-Energy, United States [grant number DE-AR0000393]. We would like to thank Jei Gyeong Jeon and Sara Ha for their help in the data collection process.

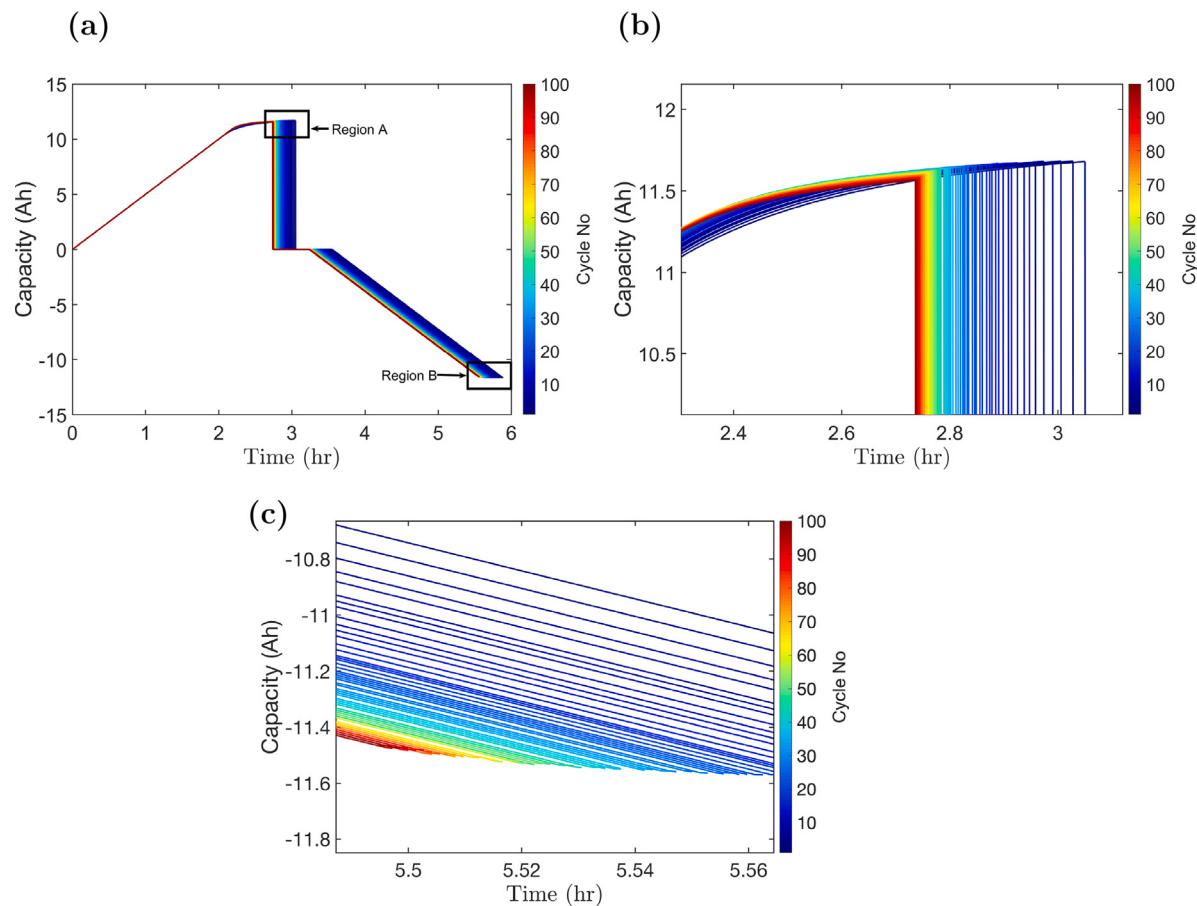


Fig. 20. The capacity profile of the battery for 100 cycles: (a) shows the capacity profile for constant current charging, constant voltage charging, rest, and the constant current discharge and how the profiles change over 100 cycles; (b) zoomed-in view of region A; (c) zoomed-in view of region B; (d) zoomed-in view of region C.

Appendix. Additional figures

See Figs. 18–20.

Data availability

Data will be made available on request.

References

- [1] A. Barré, B. Deguilhem, S. Grolleau, M. Gérard, F. Suard, D. Riu, A review on lithium-ion battery ageing mechanisms and estimations for automotive applications, *J. Power Sources* 241 (2013) 680–689.
- [2] M. Yoshio, R.J. Brodd, A. Kozawa, *Lithium-ion batteries*, vol. 1, Springer, 2009.
- [3] R. Xiong, L. Li, J. Tian, Towards a smarter battery management system: A critical review on battery state of health monitoring methods, *J. Power Sources* 405 (2018) 18–29.
- [4] Y. Wang, J. Tian, Z. Sun, L. Wang, R. Xu, M. Li, Z. Chen, A comprehensive review of battery modeling and state estimation approaches for advanced battery management systems, *Renew. Sustain. Energy Rev.* 131 (2020) 110015.
- [5] J. Hong, D. Lee, E.-R. Jeong, Y. Yi, Towards the swift prediction of the remaining useful life of lithium-ion batteries with end-to-end deep learning, *Appl. Energy* 278 (2020) 115646.
- [6] K.A. Severson, P.M. Attia, N. Jin, N. Perkins, B. Jiang, Z. Yang, M.H. Chen, M. Aykol, P.K. Herring, D. Fragedakis, et al., Data-driven prediction of battery cycle life before capacity degradation, *Nat. Energy* 4 (5) (2019) 383–391.
- [7] Y. Zhang, R. Xiong, H. He, M.G. Pecht, Long short-term memory recurrent neural network for remaining useful life prediction of lithium-ion batteries, *IEEE Trans. Veh. Technol.* 67 (7) (2018) 5695–5705.
- [8] H. Berg, *Batteries for electric vehicles: materials and electrochemistry*, Cambridge University Press, 2015.
- [9] G.S. Misyras, D.I. Doukas, T.A. Papadopoulos, D.P. Labridis, V.G. Agelidis, State-of-charge estimation for li-ion batteries: A more accurate hybrid approach, *IEEE Trans. Energy Convers.* 34 (1) (2018) 109–119.
- [10] M. Ouyang, G. Liu, L. Lu, J. Li, X. Han, Enhancing the estimation accuracy in low state-of-charge area: A novel onboard battery model through surface state of charge determination, *J. Power Sources* 270 (2014) 221–237.
- [11] R. Xiong, J. Cao, Q. Yu, H. He, F. Sun, Critical review on the battery state of charge estimation methods for electric vehicles, *Ieee Access* 6 (2017) 1832–1843.
- [12] C. Zhang, X. Li, W. Chen, G.G. Yin, J. Jiang, et al., Robust and adaptive estimation of state of charge for lithium-ion batteries, *IEEE Trans. Ind. Electron.* 62 (8) (2015) 4948–4957.
- [13] S. Lee, J. Kim, J. Lee, B.H. Cho, State-of-charge and capacity estimation of lithium-ion battery using a new open-circuit voltage versus state-of-charge, *J. Power Sources* 185 (2) (2008) 1367–1373.
- [14] F. Zheng, Y. Xing, J. Jiang, B. Sun, J. Kim, M. Pecht, Influence of different open circuit voltage tests on state of charge online estimation for lithium-ion batteries, *Appl. Energy* 183 (2016) 513–525.
- [15] J. Lee, O. Nam, B. Cho, Li-ion battery SOC estimation method based on the reduced order extended Kalman filtering, *J. Power Sources* 174 (1) (2007) 9–15.
- [16] S. Piller, M. Perrin, A. Jossen, Methods for state-of-charge determination and their applications, *J. Power Sources* 96 (1) (2001) 113–120.
- [17] N. Yang, X. Zhang, G. Li, State-of-charge estimation for lithium ion batteries via the simulation of lithium distribution in the electrode particles, *J. Power Sources* 272 (2014) 68–78.
- [18] W. Yang, H. Xie, B. Shi, H. Song, W. Qiu, Q. Zhang, In-situ experimental measurements of lithium concentration distribution and strain field of graphite electrodes during electrochemical process, *J. Power Sources* 423 (2019) 174–182.
- [19] G.K. Prasad, C.D. Rahn, Model based identification of aging parameters in lithium ion batteries, *J. Power Sources* 232 (2013) 79–85.
- [20] D. Di Domenico, G. Fiengo, A. Stefanopoulou, Lithium-ion battery state of charge estimation with a kalman filter based on a electrochemical model, in: 2008 IEEE International Conference on Control Applications, Ieee, 2008, pp. 702–707.
- [21] Y. Bi, Y. Yin, S.-Y. Choe, Online state of health and aging parameter estimation using a physics-based life model with a particle filter, *J. Power Sources* 476 (2020) 228655.

- [22] R.R. Richardson, M.A. Osborne, D.A. Howey, Gaussian process regression for forecasting battery state of health, *J. Power Sources* 357 (2017) 209–219.
- [23] A. Marongiu, N. Nlandi, Y. Rong, D.U. Sauer, On-board capacity estimation of lithium iron phosphate batteries by means of half-cell curves, *J. Power Sources* 324 (2016) 158–169.
- [24] J. Guo, Z. Li, M. Pecht, A Bayesian approach for li-ion battery capacity fade modeling and cycles to failure prognostics, *J. Power Sources* 281 (2015) 173–184.
- [25] J. Li, R.G. Landers, J. Park, A comprehensive single-particle-degradation model for battery state-of-health prediction, *J. Power Sources* 456 (2020) 227950.
- [26] S. Amir, M. Gulzar, M.O. Tarar, I.H. Naqvi, N.A. Zaffar, M.G. Pecht, Dynamic equivalent circuit model to estimate state-of-health of lithium-ion batteries, *IEEE Access* 10 (2022) 18279–18288.
- [27] L. Chen, X. Bao, A.M. Lopes, C. Xu, X. Wu, H. Kong, S. Ge, J. Huang, State of health estimation of lithium-ion batteries based on equivalent circuit model and data-driven method, *J. Energy Storage* 73 (2023) 109195.
- [28] Z. Huang, M. Best, J. Knowles, A. Fly, Adaptive piecewise equivalent circuit model with SOC/SOH estimation based on extended Kalman filter, *IEEE Trans. Energy Convers.* 38 (2) (2022) 959–970.
- [29] H. Dong, X. Jin, Y. Lou, C. Wang, Lithium-ion battery state of health monitoring and remaining useful life prediction based on support vector regression-particle filter, *J. Power Sources* 271 (2014) 114–123.
- [30] S. Jenu, A. Hentunen, J. Haavisto, M. Pihlatie, State of health estimation of cycle aged large format lithium-ion cells based on partial charging, *J. Energy Storage* 46 (2022) 103855.
- [31] Z. Chen, H. Zhao, Y. Zhang, S. Shen, J. Shen, Y. Liu, State of health estimation for lithium-ion batteries based on temperature prediction and gated recurrent unit neural network, *J. Power Sources* 521 (2022) 230892.
- [32] Y. Ma, C. Shan, J. Gao, H. Chen, A novel method for state of health estimation of lithium-ion batteries based on improved LSTM and health indicators extraction, *Energy* 251 (2022) 123973.
- [33] Z. Sherkatghanad, A. Ghazanfari, V. Makarenkov, A self-attention-based CNN-Bi-LSTM model for accurate state-of-charge estimation of lithium-ion batteries, *J. Energy Storage* 88 (2024) 111524.
- [34] C. Zhang, L. Tu, Z. Yang, B. Du, Z. Zhou, J. Wu, L. Chen, A CMMOG-based lithium-battery SOH estimation method using multi-task learning framework, *J. Energy Storage* 107 (2025) 114884.
- [35] K.-W. Nam, S.-M. Bak, E. Hu, X. Yu, Y. Zhou, X. Wang, L. Wu, Y. Zhu, K.-Y. Chung, X.-Q. Yang, Combining *in situ* synchrotron X-ray diffraction and absorption techniques with transmission electron microscopy to study the origin of thermal instability in overcharged cathode materials for lithium-ion batteries, *Adv. Funct. Mater.* 23 (8) (2013) 1047–1063.
- [36] N. Sharma, V.K. Peterson, M.M. Elcombe, M. Avdeev, A.J. Studer, N. Blagojevic, R. Yusoff, N. Kamarulzaman, Structural changes in a commercial lithium-ion battery during electrochemical cycling: An *in situ* neutron diffraction study, *J. Power Sources* 195 (24) (2010) 8258–8266.
- [37] U. Tröltzsch, O. Kanoun, H.-R. Tränkler, Characterizing aging effects of lithium ion batteries by impedance spectroscopy, *Electrochim. Acta* 51 (8–9) (2006) 1664–1672.
- [38] W. Waag, S. Käbitz, D.U. Sauer, Experimental investigation of the lithium-ion battery impedance characteristic at various conditions and aging states and its influence on the application, *Appl. Energy* 102 (2013) 885–897.
- [39] J.B. Robinson, M. Pham, M.D. Kok, T.M. Heenan, D.J. Brett, P.R. Shearing, Examining the cycling behaviour of li-ion batteries using ultrasonic time-of-flight measurements, *J. Power Sources* 444 (2019) 227318.
- [40] L. Oca, N. Guillet, R. Tessard, U. Iraola, Lithium-ion capacitor safety assessment under electrical abuse tests based on ultrasound characterization and cell opening, *J. Energy Storage* 23 (2019) 29–36.
- [41] Y.-S. Chou, N.-Y. Hsu, K.-T. Jeng, K.-H. Chen, S.-C. Yen, A novel ultrasonic velocity sensing approach to monitoring state of charge of vanadium redox flow battery, *Appl. Energy* 182 (2016) 253–259.
- [42] G. Davies, K.W. Knehr, B. Van Tassell, T. Hodson, S. Biswas, A.G. Hsieh, D.A. Steingart, State of charge and state of health estimation using electrochemical acoustic time of flight analysis, *J. Electrochem. Soc.* 164 (12) (2017) A2746.
- [43] Y. Wu, Y. Wang, W.K. Yung, M. Pecht, Ultrasonic health monitoring of lithium-ion batteries, *Electronics* 8 (7) (2019) 751.
- [44] L. Gold, T. Bach, W. Virsik, A. Schmitt, J. Müller, T.E. Staab, G. Sextl, Probing lithium-ion batteries' state-of-charge using ultrasonic transmission-concept and laboratory testing, *J. Power Sources* 343 (2017) 536–544.
- [45] H. Popp, M. Koller, S. Keller, G. Glanz, R. Klambauer, A. Bergmann, State estimation approach of lithium-ion batteries by simplified ultrasonic time-of-flight measurement, *IEEE Access* 7 (2019) 170992–171000.
- [46] Z. Deng, Z. Huang, Y. Shen, Y. Huang, H. Ding, A. Luscombe, M. Johnson, J.E. Harlow, R. Gauthier, J.R. Dahn, Ultrasonic scanning to observe wetting and “unwetting” in li-ion pouch cells, *Joule* 4 (9) (2020) 2017–2029.
- [47] C. Bommier, W. Chang, Y. Lu, J. Yeung, G. Davies, R. Mohr, M. Williams, D. Steingart, In operando acoustic detection of lithium metal plating in commercial LiCoO₂/graphite pouch cells, *Cell Rep. Phys. Sci.* 1 (4) (2020).
- [48] M. Koller, G. Glanz, A. Bergmann, H. Popp, Determination of lamb wave modes on lithium-ion batteries using piezoelectric transducers, *Sensors* 22 (13) (2022) 4748.
- [49] S. Ahmed, F. Kopsaftopoulos, Stochastic identification of guided wave propagation under ambient temperature via non-stationary time series models, *Sensors* 21 (16) (2021) 5672.
- [50] S. Ahmed, F. Kopsaftopoulos, Active sensing acousto-ultrasound SHM via stochastic non-stationary time series models, in: European Workshop on Structural Health Monitoring, Springer, 2022, pp. 256–266.
- [51] S. Ahmed, F. Kopsaftopoulos, Statistical active-sensing structural health monitoring via stochastic time-varying time series models, in: 2022 American Control Conference, ACC, IEEE, 2022, pp. 3599–3606.
- [52] K. Graff, Wave motion in elastic solids, Dover Books on Physics Series, Dover Publications, 1991.
- [53] R. Copley, D. Cumming, Y. Wu, R. Dwyer-Joyce, Measurements and modelling of the response of an ultrasonic pulse to a lithium-ion battery as a precursor for state of charge estimation, *J. Energy Storage* 36 (2021) 102406.
- [54] K.W. Knehr, T. Hodson, C. Bommier, G. Davies, A. Kim, D.A. Steingart, Understanding full-cell evolution and non-chemical electrode crosstalk of li-ion batteries, *Joule* 2 (6) (2018) 1146–1159.
- [55] A. Hsieh, S. Bhadra, B. Hertzberg, P. Gjeltema, A. Goy, J.W. Fleischer, D.A. Steingart, Electrochemical-acoustic time of flight: in operando correlation of physical dynamics with battery charge and health, *Energy & Environ. Sci.* 8 (5) (2015) 1569–1577.
- [56] P. Ladpli, F. Kopsaftopoulos, F.-K. Chang, Estimating state of charge and health of lithium-ion batteries with guided waves using built-in piezoelectric sensors/actuators, *J. Power Sources* 384 (2018) 342–354.
- [57] J.M. Hooper, J. Marco, Experimental modal analysis of lithium-ion pouch cells, *J. Power Sources* 285 (2015) 247–259.
- [58] H.L. Pham, J.E. Dietz, D.E. Adams, N.D. Sharp, Lithium-ion battery cell health monitoring using vibration diagnostic test, in: ASME International Mechanical Engineering Congress and Exposition, Vol. 56253, American Society of Mechanical Engineers, 2013, V04BT04A048.
- [59] H. Popp, G. Glanz, K. Alten, I. Gocheva, W. Berghold, A. Bergmann, Mechanical frequency response analysis of lithium-ion batteries to disclose operational parameters, *Energies* 11 (3) (2018) 541.
- [60] S. Ahmed, F. Kopsaftopoulos, Active sensing ultrasonic guided wave-based damage diagnosis via stochastic stationary time-series models, *Struct. Heal. Monit.* (2023) 14759217231201975.
- [61] H. Le Pham, Health diagnosis of lithium-ion battery cell using vibration-based test and analysis (Ph.D. thesis), Purdue University, 2013.
- [62] R. Xu, H. Sun, L.S. de Vasconcelos, K. Zhao, Mechanical and structural degradation of LiNi_xMn_yCo_zO₂ cathode in li-ion batteries: an experimental study, *J. Electrochem. Soc.* 164 (13) (2017) A3333.
- [63] K. Kganyago, P. Ngope, Structural and electronic properties of lithium intercalated graphite LiC₆, *Phys. Rev. B* 68 (20) (2003) 205111.
- [64] H. Zheng, L. Zhang, G. Liu, X. Song, V.S. Battaglia, Correlationship between electrode mechanics and long-term cycling performance for graphite anode in lithium ion cells, *J. Power Sources* 217 (2012) 530–537.